

Chapter 4

RESULTS AND DISCUSSION

Various characterization methods have been used to evaluate the mechanical and microstructural properties of prepared samples. The characterization of composites is very important part to check the quality of the materials as per the industrial requirements. By performing various characterizations, researchers can get ideas for development the new materials as per the global need. In present research work, phase wise results are shown and discussed.

4.1 Raw materials analysis

Chemical compositions of raw materials in as received condition are as shown in table 4.1. CPA contains various other elements like Si, Mn, Mg, Fe, Cu and Zn. Fe amount was found maximum as compared to other impurity elements. Magnesium metal has Si and Al as an impurity. Analysis of as received CPA and Mg were carried out by spectroscopy test whereas for MnO_2 , both EDS and XRD analysis were carried out. The XRD Patterns of as received commercially pure aluminium and MnO_2 are as given in figure 4.1(a) and figure 4.1(b).

Table 4.1: Chemical composition of as supplied raw materials by Energy Dispersive Spectroscopy (EDS)

Elements (wt %)	Si	Mn	Mg	Fe	Cu	Zn	C	O	K	Al
<i>CP Aluminium</i>	0.05	0.02	0.03	0.42	0.05	0.04	–	–	–	99.39
<i>Magnesium</i>	0.13	–	99.68	–	–	–	–	–	–	0.19
<i>MnO₂ Powder</i>	0.81	51.68	–	3.09	–	–	7.6	35.56	0.82	0.51

The purpose of XRD analysis and microstructural analysis of as received commercially pure aluminium and MnO_2 were to confirm pre existing impurities and phases in the materials. It was found the presence of complex Fe-Mn carbide and Fe-Si phase along with $\beta - MnO_2$ as shown in figure 4.1. Result indicates the MnO_2 powder consists of $\beta - MnO_2$ and k-type of iron manganese carbide $(Fe_{0.6}Mn_{5.4}C_2)_{10}$. The presence of $(Fe_{0.6}Mn_{5.4}C_2)_{10}$ phase changes the decomposition behaviour of the MnO_2 powder. No other impurities were detected in the as received MnO_2 powder. Figure 4.2 indicates of microstructure of as received commercially pure aluminium and SEM image of as received MnO_2 powder at 100X magnification.

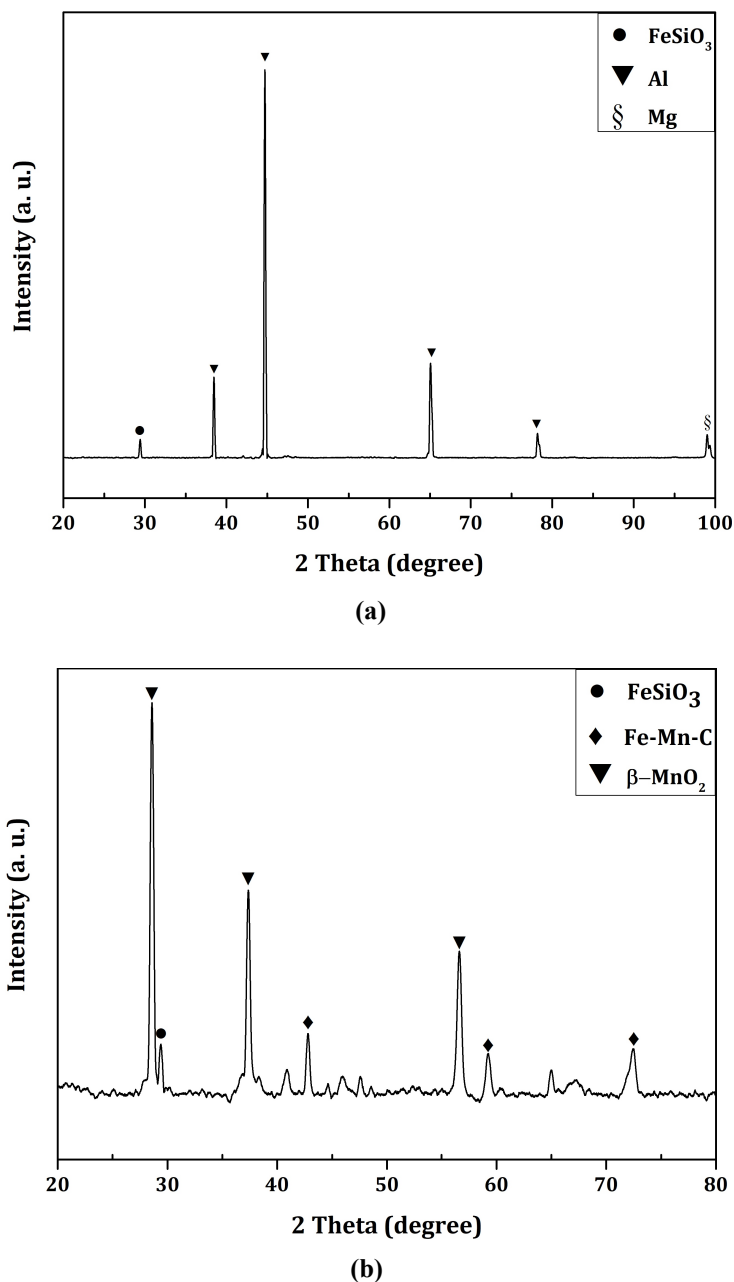


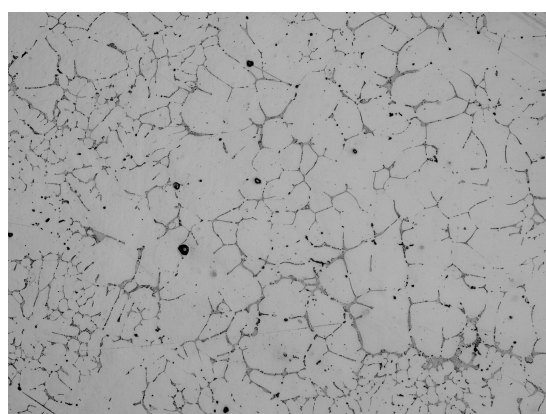
Figure 4.1: Typical XRD pattern of (a) Commercially Pure Aluminium (CPA) and (b) MnO_2 powder in as received condition.

Table 4.2: X-Ray diffraction values of as received commercially pure aluminium.

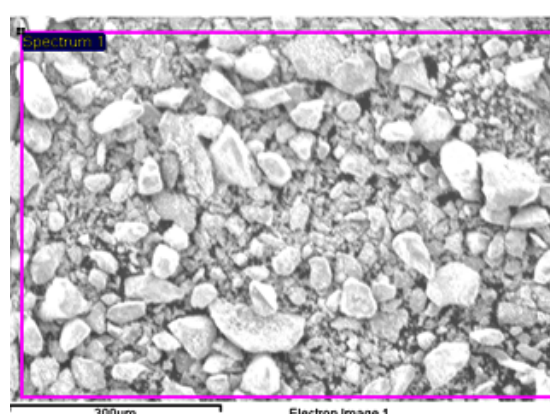
Sr. No.	2-Theta	Observed d value	Phase	JCPDS Card No.
1	29.40	3.03	$FeSiO_3$	17 – 548
2	29.38	2.33	Al	4 – 787
3	44.69	2.02	Al	4 – 787
4	65.06	1.43	Al	4 – 787
5	78.19	1.22	Al	4 – 787
6	99.01	1.01	Mg	4 – 770

Table 4.3: X-Ray diffraction values of as received MnO_2 powder.

Sr. No.	2-Theta	Observed d value	Phase	JCPDS Card No.
1	28.60	3.11	$\beta-MnO_2$	24 – 735
2	29.38	3.03	$FeSiO_3$	17 – 548
3	37.30	2.40	$\beta-MnO_2$	24 – 735
4	42.73	2.11	$(Fe_{0.6}Mn_{5.4}C_2)_{10}$	20 – 521
5	56.58	1.62	$\beta-MnO_2$	24 – 735
6	59.16	1.56	$(Fe_{0.6}Mn_{5.4}C_2)_{10}$	20 – 521
7	72.39	1.30	$(Fe_{0.6}Mn_{5.4}C_2)_{10}$	20 – 521



(a)



(b)

Figure 4.2: (a) Optical microstructure of Commercially Pure Aluminium (CPA) and (b) SEM image of MnO_2 powder at 100X.

The size of MnO_2 powder used during this investigation was in the range of 75 to less than 44 micron. This size is considered as idea for making particulate reinforced metal matrix composite. The size analysis was performed by standard sieve analysis. Table 4.4 is indicating the results of sieve analysis.

Table 4.4: Sieve analysis of MnO_2 powder.

Sr. No.	BSS Mesh Number	Size (micron)	Content (wt %)
1	-60 +100	150	0.143
2	-100 +120	125	0.291
3	-120 +150	100	0.073
4	-150 +200	75	13.326
5	-200 +300	53	23.259
6	-300 +350	44	17.902
7	PAN	–	41.916

4.2 Composite materials analysis

The analyses of prepared composite samples were carried out in following sequence:

1. Chemical analysis (Element recovery analysis)
2. X-Ray diffraction analysis
3. Density and ductility analysis
4. Hardness and strength analysis
5. Microstructure analysis

4.2.1 Phase I: Effect of weight percentage of magnesium in CPA

Addition of magnesium into aluminium imparts its strength without adversely affecting existing properties of the base metal. Various applications found for aluminium magnesium alloys such as train bodies, truck bodies, engines, armoured vehicles, building construction parts, pressure vessels, chemical containers, ships, etc. Along with silicon, Al-Mg system shows drastic benefits in terms of mechanical properties.

In phase I, as discussed in chapter 3, optimization analysis for magnesium was carried out using different amount of magnesium into CPA so in further experiments in phase III, optimised magnesium amount can be used to get best results. Different characterization methods were used to find out Al-Mg properties as discussed below.

1. Chemical Analysis

Table 4.5 shows spectroscopy results of different experiments of Al-Mg system. Different elements like O, Mg, Si, Mn and Fe were observed and presented in following table. As the weight percentage of magnesium was increased, the recovery was also increased. At the same time, amount of oxygen was reduced. The amount of trace elements like Si, Mn and Fe were found minimum. Due to the presence of different elements, the presence of various phases were confirmed. Magnesium is strengthening element which forms solid solution strengthening into the CPA matrix. Hence it has improved various mechanical properties as discussed in following sections.

Table 4.5: Chemical compositions of various Al-Mg systems by spectroscopy (Element Recovery).

Experiments	Mg added (wt %)	Element Composition (wt %)					
		<i>Mg Recovered</i>	<i>Mn</i>	<i>Si</i>	<i>Fe</i>	<i>O</i>	<i>Al</i>
1	0.00	0.05	0.015	0.27	0.37	14.2	85.095
2	0.05	0.04	0.017	0.15	0.46	11.2	88.133
3	0.15	0.13	0.022	0.35	0.39	10.1	89.008
4	0.5	0.1	0.019	0.14	0.33	8.14	91.271
5	1	0.66	0.021	0.33	0.45	7.79	90.749
6	1.5	1.46	0.023	0.33	0.41	9.8	87.977
7	2	2.02	0.016	0.21	0.53	12	85.224
8	3	2.67	0.014	0.34	0.49	7.28	89.20
9	4	3.71	0.024	0.16	0.46	7.35	88.296
10	5	4.13	0.013	0.22	0.57	5.19	89.877
11	6	5.77	0.022	0.44	0.61	4.51	88.648
12	7	6.87	0.026	0.36	0.31	3.77	88.664

From above table, we can see variations of different chemical elements in Al-Mg metal. Magnesium was varied from 0.05 wt % to 7 wt %. In the resultant cast composite, analysis of O, Mg, Si, Mn, Fe and Al was made by spectroscopy.

2. X-Ray Diffraction

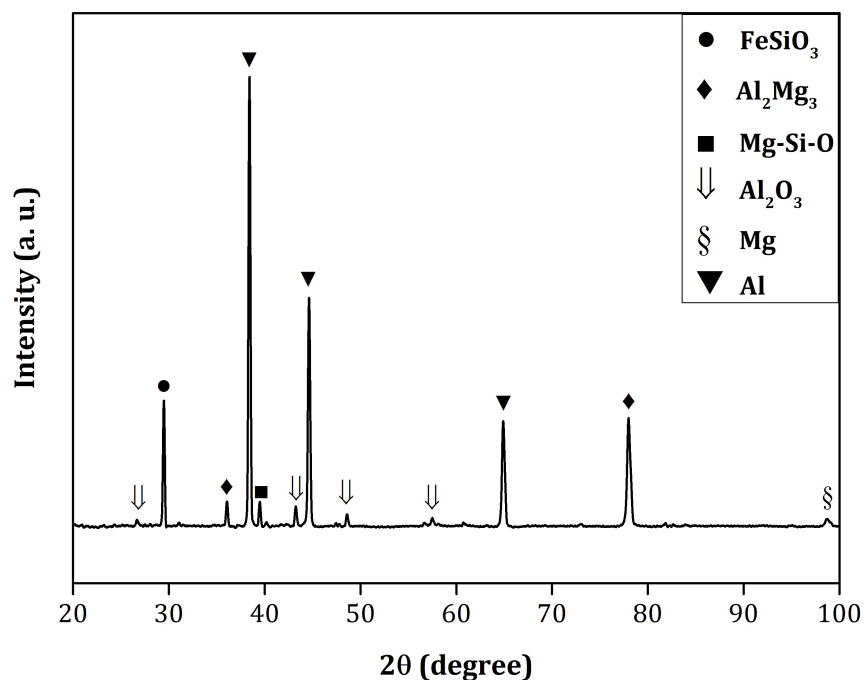


Figure 4.3: Typical XRD pattern of Al-3 wt % Mg system.

Table 4.6: X-Ray diffraction values of Al-3 wt % Mg sample.

Sr. No.	2-Theta	Observed d value	Phase	JCPDS Card No.
1	26.67	3.33	Al_2O_3	10 – 173
2	29.45	3.03	$FeSiO_3$	17 – 548
3	36.02	2.49	Al_2Mg_3	1 – 1128
4	38.37	2.33	Al	4 – 787
5	39.43	2.28	$Mg - Si - O$	22 – 1216
6	43.20	2.09	Al_2O_3	10 – 173
7	44.61	2.02	Al	4 – 787
8	48.58	1.87	Al_2O_3	10 – 173
9	57.48	1.60	Al_2O_3	10 – 173
10	64.91	1.44	Al_2Mg_3	1 – 1128
11	77.99	1.22	Al	4 – 787
12	98.75	1.01	Mg	4 – 770

X-ray diffraction analysis of Al-3 wt % Mg system was carried out as it was showing maximum values of properties especially the strength as discussed later. The typical XRD graph is shown in figure 4.3. As listed in table 4.6, presence of $MgSiO_3$, Al_2Mg_3 , $Mg - Si - O$, Al_2O_3 and free Mg phases were confirmed. These in-situ phases were generated into the CPA matrix at processing temperature. Due to the presence of these multi in-situ phases, different mechanical properties were increased.

3. Density and ductility

As shown in graph below (figure 4.4), the density and ductility both reduced as magnesium concentration increased.

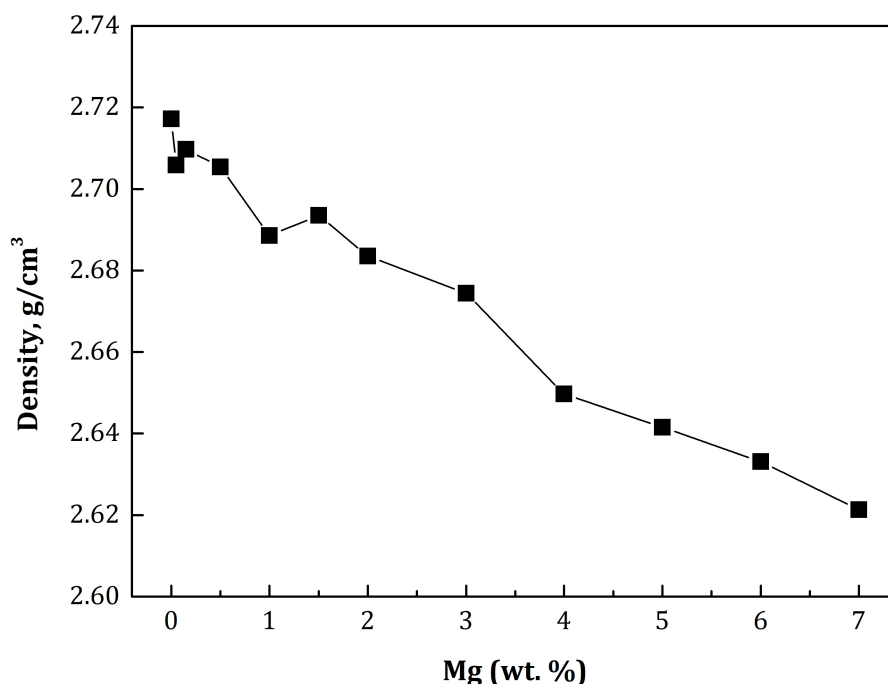


Figure 4.4: Variation of density in Al-Mg system.

Density is very important criteria for selection of the alloy for light weight and high performance application such as aerospace and automotive industries. Elements like magnesium, lithium and silicon decrease the density whereas chromium, copper, iron, manganese, nickel, titanium and zinc increase it. Density of the composites also affects by porosity, macrosegregation, degree of solid solution, fabrication of products, etc [John E. Hetch]. In present study, the density of the system was found decreasing throughout the variations of magnesium addition in CPA due to increasing the concentration of Mg which is having lower density (1.74 gm/cm^3) compared to that of the aluminium (2.7 gm/cm^3).

As shown in figure 4.5, ductility in terms of percentage elongation and reduction in area were measured as discussed in chapter 3 in as-cast condition. Ductility of overall system was also decreased as concentration of magnesium increased like the density as discussed above. This was due to formation of brittle phases such as oxides and carbides into the Al-Mg system as stated in microstructural analysis. Such phases are although light in weight but brittle in nature. Upon plastic deformation of the sample, such phases break into fine angular particles and act as stress raiser in the matrix. Hence as compared to the base metal, the ductility was not improved.

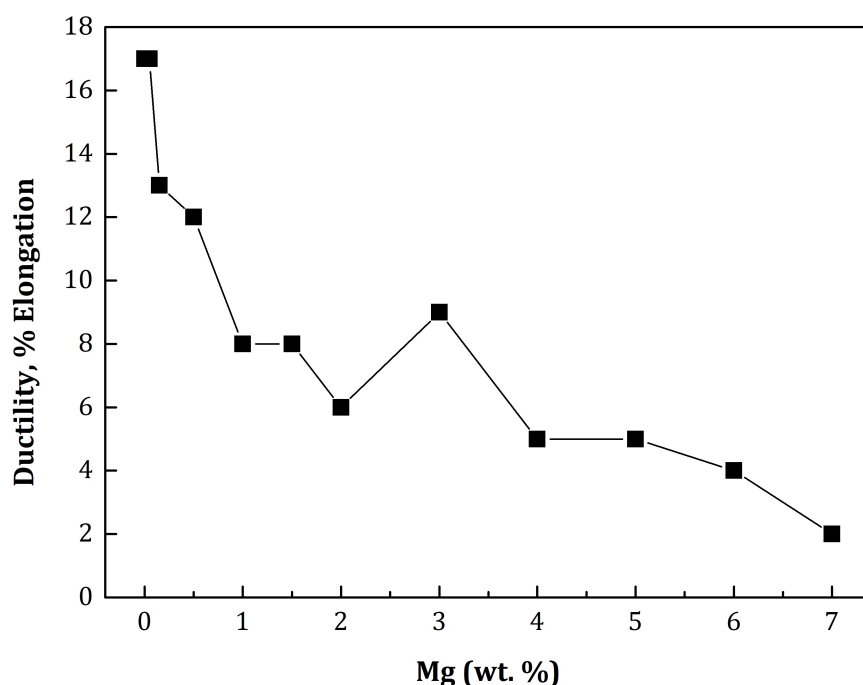


Figure 4.5: Variation of ductility in Al-Mg system.

4. Hardness and strength

Normally strength and hardness decreases with purity of the metal increases. More amount of the cold working can increase strength of the metal due to work hardening whereas the higher iron-silicon ratio can adversely affect these properties. Strength and hardness values have inverse relations in general. But in this work, hardness trend was found increasing starting from the initial experiments upto 3 wt % Mg as shown in figure 4.6. After 3 wt % Mg, hardness continued to increase although strength dropped.

As we can observe from the figure 4.7, the ultimate tensile strength was found increasing initially and attained maximum value at 3 wt % of magnesium concentration. At 3 wt% Mg, highest UTS was achieved almost 217 MPa as compared to 115 MPa in base metal CPA. UTS value decreased to 167 MPa in 7 wt % of magnesium addition. Hence specific strength, i.e., strength to density ratio also increased from $42 \text{ kN} - \text{m}/\text{kg}$ of base metal

to $81 \text{ kN} - \text{m/kg}$ at 3 wt % Mg and then decreased to $64 \text{ kN} - \text{m/kg}$ at 7 wt % of magnesium concentration. After 4 wt % of magnesium, the slope of the graph became almost steady. Due to the formation of various intermetallics phases into the CPA matrix, strength was found increasing as compared to the base metal alone. As solubility of magnesium into aluminium decreases below 100°C , the solid solution strengthening effect can be observed maximum at 3 wt % of magnesium as compared to different experiments in this Al-Mg system.

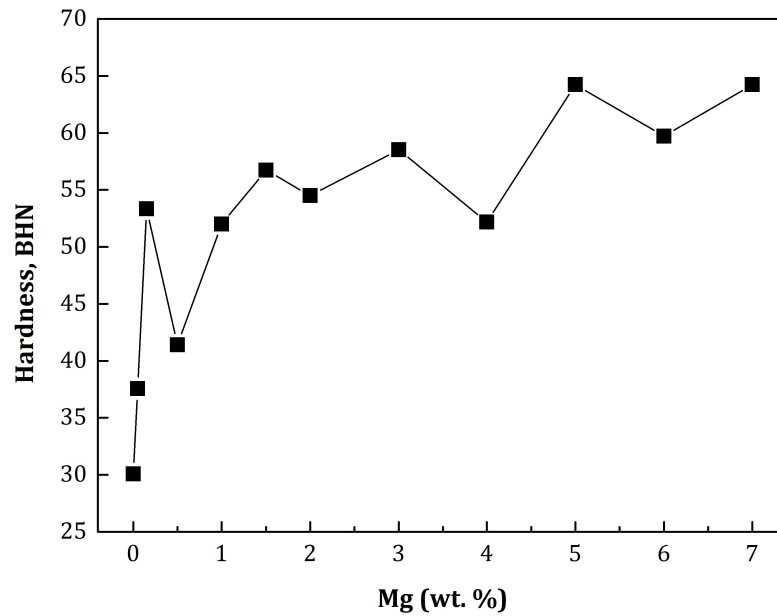


Figure 4.6: Variation of the hardness in Al-Mg system.

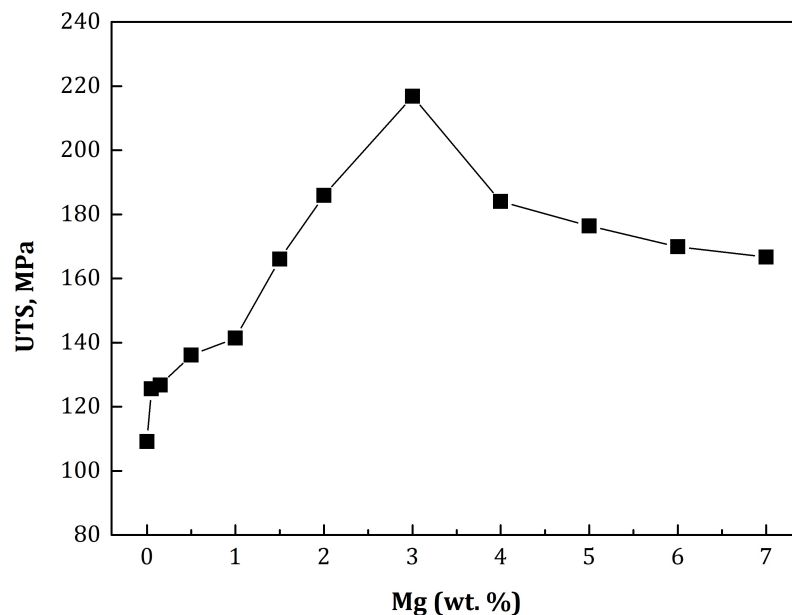


Figure 4.7: Variation of the ultimate tensile strength in Al-Mg system.

5. Microstructure Analysis

As discussed in chapter 3, samples for microstructure analysis were prepared by following standard metallographic technique with no etching. Optical microstructures are shown in figure 4.8 and 4.9 and Scanning Electron Microscope (SEM) images are shown in figure 4.10 and 4.11.

By increasing of magnesium amount unreacted Mg is observed at the grain boundaries along with other intermetallic phases. This leads to change in the morphology of the grain structure. Due to formation of various solidification front, engulfment and pushing effects are responsible for the gathering of these micro particles at the grain boundaries. Such engulfment and pushing effect was nominal up to 3 wt % of Mg and increased significantly after 3 wt % of Mg. Heavy cluster of intermetallic phases were observed in 4 wt %, 5 wt %, 6 wt % and 7 wt % of Mg as shown in figure 4.9. Unreacted Mg also increased due to the limited solubility of Mg metal in aluminium. Below 100 °C, the solubility of Mg reduces and becomes less than 3 wt %. But above 300 °C, even 7 wt % Mg can be dissolved in aluminium melt easily as per the equilibrium phase diagram of Al-Mg. In this work, 3 wt % Mg can help to improve the wettability of the resulting in-situ intermetallic phases.

Microstructures of the Al-Mg system show flawless grain structures. Intermetallics shown in microstructures are already written in table 4.6 which are confirmed by XRD analysis. The columnar grains were absent in the microstructures and equiaxed grains are present. This is due to slow cooling rate as die was preheated before pouring. Microstructure of 3 wt % Mg is more uniform and equiaxed as compare to other microstructures. As the amount of Mg increased, free Mg was found in the structure as dark black phase (figure 4.11d and 4.11e).

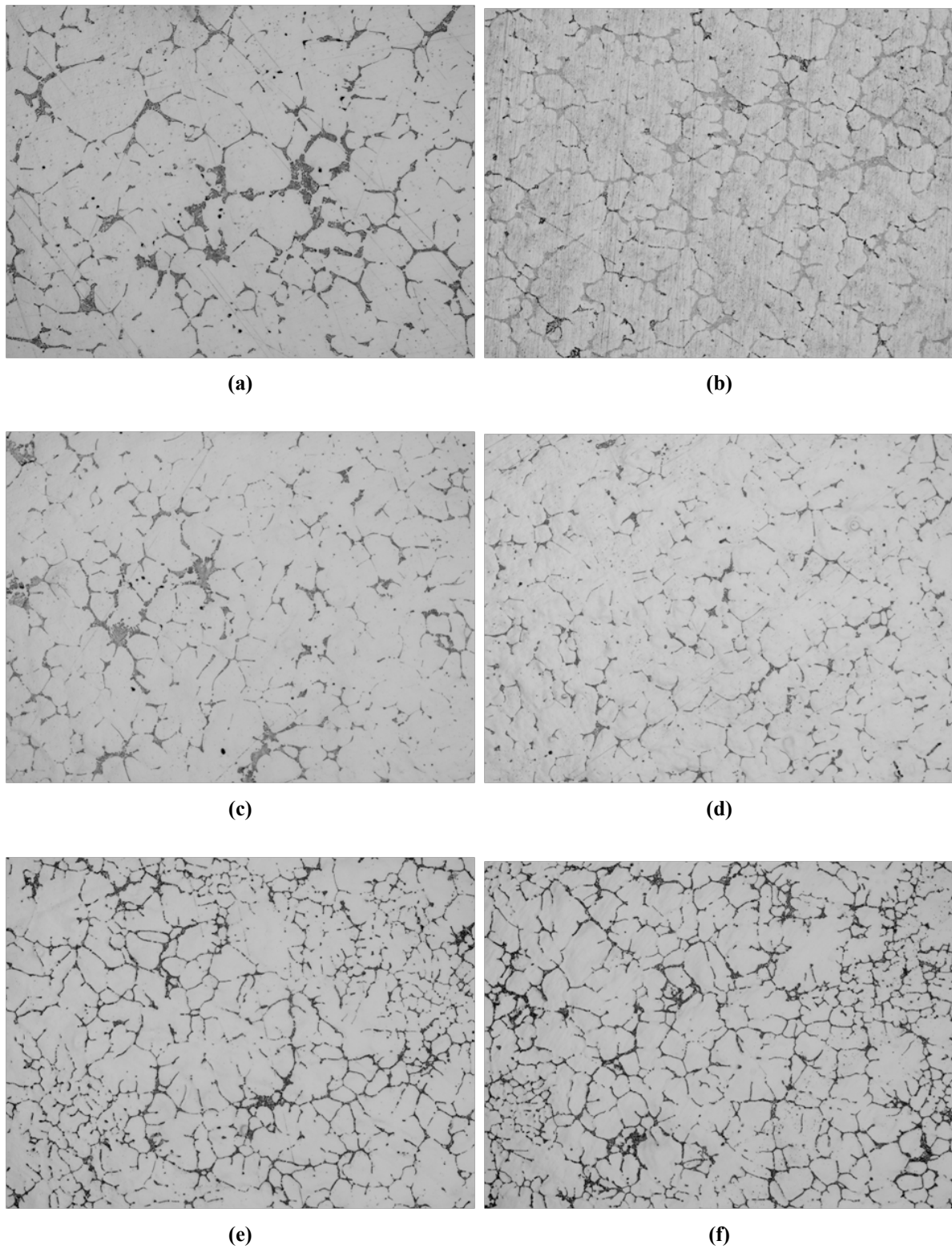


Figure 4.8: Optical Microstructure of (a) 0.05 wt % Mg, (b) 0.15 wt % Mg, (c) 0.5 wt % Mg, (d) 1 wt % Mg, (e) 1.5 wt % Mg, and (f) 2 wt % Mg of Al-Mg system at 100x magnification (Without Etching).

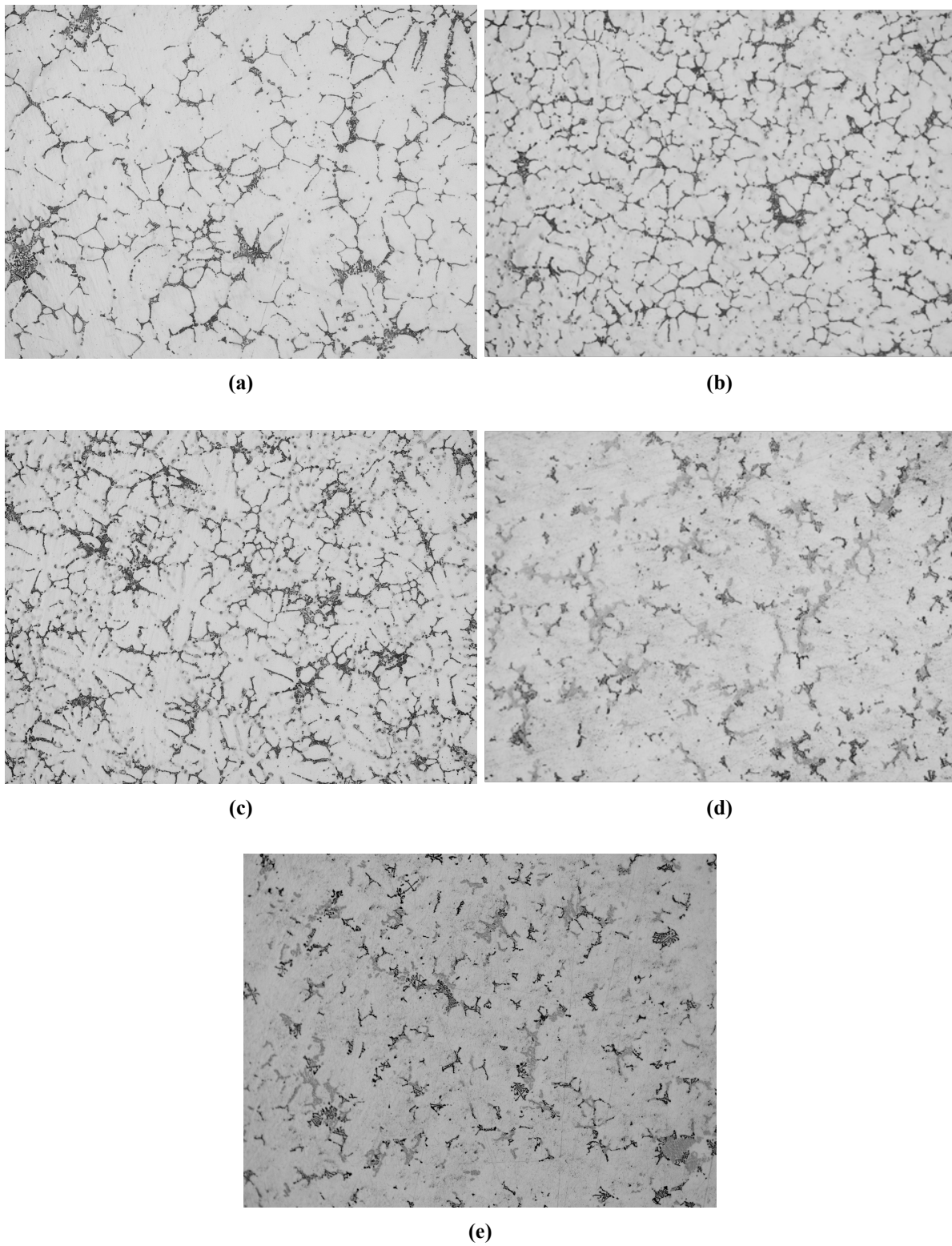


Figure 4.9: Optical Microstructure of (a) 3 wt % Mg, (b) 4 wt % Mg, (c) 5 wt % Mg, (d) 6 wt % Mg and (e) 7 wt % Mg of Al-Mg system at 100x magnification (Without Etching).

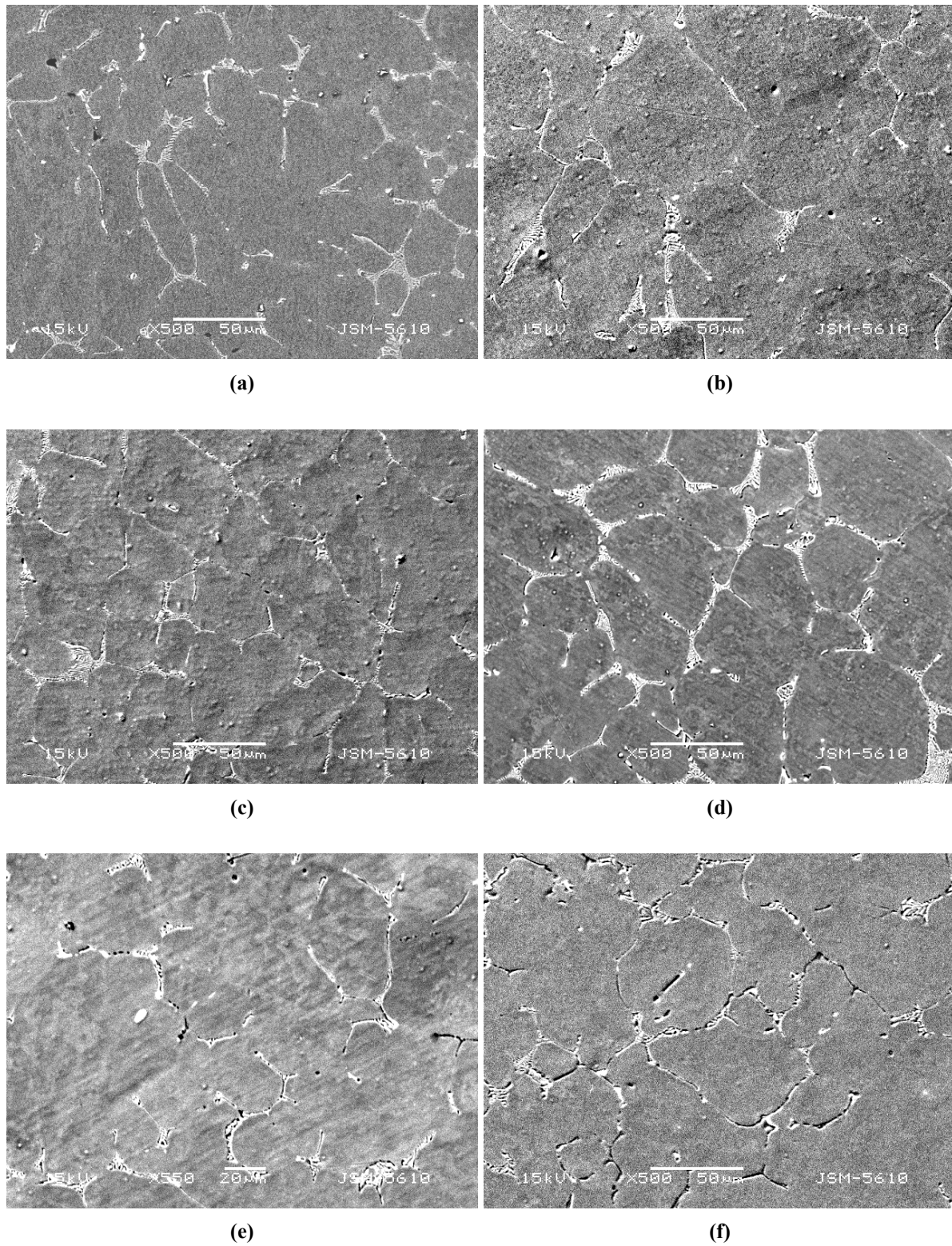


Figure 4.10: SEM images of (a) 0.05 wt % Mg, (b) 0.15 wt % Mg, (c) 0.5 wt % Mg, (d) 1 wt % Mg, (e) 1.5 wt % Mg, and (f) 2 wt % Mg of Al-Mg system at 500x magnification (Without Etching).

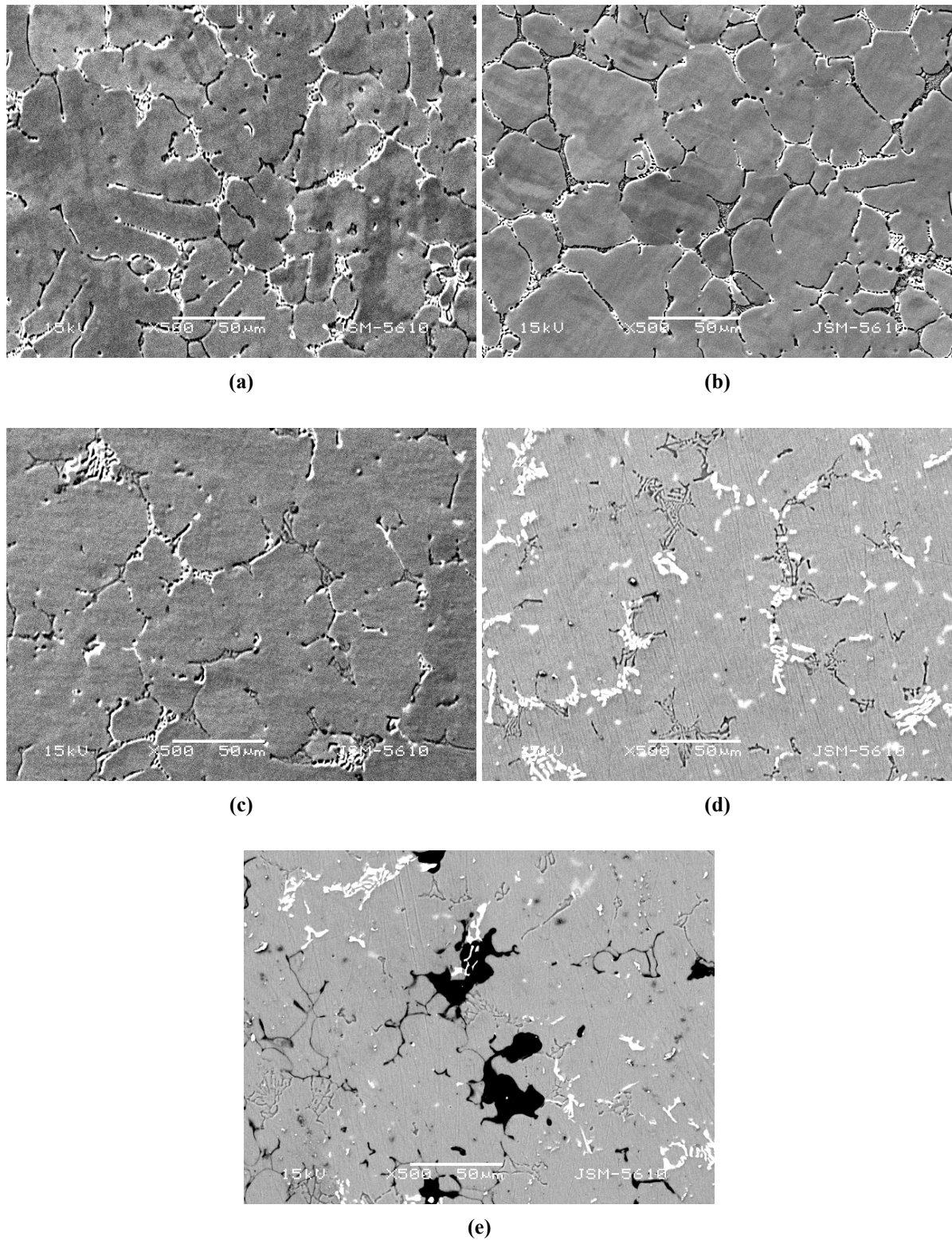


Figure 4.11: SEM images of (a) 3 wt % Mg, (b) 4 wt % Mg, (c) 5 wt % Mg, (d) 6 wt % Mg and (e) 7 wt % Mg of Al-Mg system at 500x magnification (Without Etching).

4.2.2 Phase II: Effect of variation of MnO_2 by changing its addition sequence in CPA

In phase II experiments, optimisation of MnO_2 was carried out without addition of magnesium into CPA. MnO_2 has decomposition point below $600\text{ }^\circ\text{C}$ i.e., at $535\text{ }^\circ\text{C}$ [134] and it decomposes into manganese and oxygen as discussed in chapter 2. The available manganese and oxygen in liquid aluminium bath react with various elements present and form difference phases. Various characterizations were performed to evaluate the final properties of $Al - MnO_2$ system as discussed below.

1. Chemical analysis

Table 4.7: Chemical compositions of various $Al - MnO_2$ systems by spectroscopy (Element Recovery)

Experiments	MnO_2 added (wt %)	Element Composition (wt %)				
		Mn Recovered	Si	Fe	O	Al
<i>Sequence A*</i>						
1	0.5	0.20	0.42	0.28	3.71	95.11
2	1	0.24	0.74	0.61	3.67	94.99
3	1.5	0.32	0.68	0.54	3.87	94.51
4	2	0.20	0.71	0.46	3.29	95.38
5	2.5	0.14	0.72	0.33	3.00	95.56
6	3	0.24	0.83	0.47	3.45	95.00
7	3.5	0.23	0.75	0.54	3.65	94.95
8	4	0.19	0.67	0.54	3.12	95.56
<i>Sequence B[#]</i>						
9	0.5	0.26	0.63	0.30	3.53	94.92
10	1	0.27	0.70	0.45	3.21	95.20
11	1.5	0.36	0.74	0.52	3.72	94.76
12	2	0.31	0.86	0.43	3.86	94.68
13	2.5	0.29	0.77	0.21	3.69	94.73
14	3	0.47	0.72	0.27	3.54	94.94
15	3.5	0.32	0.82	0.35	3.42	95.05
16	4	0.33	0.78	0.53	3.77	94.74

*Sequence A: MnO_2 added after melting of commercially pure aluminium and

[#]Sequence B: MnO_2 added before melting of commercially pure aluminium

Recovery of manganese was found highest in 2.5 wt % MnO_2 of sequence B as shown in figure 4.12. As mentioned earlier, presence of iron and silicon affects the mechanical properties. Figure shows the variation of iron and silicon ratio with respect to wt % MnO_2 added. It has been observed that Fe/Si ratio was found lowest in 2.5 wt % MnO_2 of sequence B.

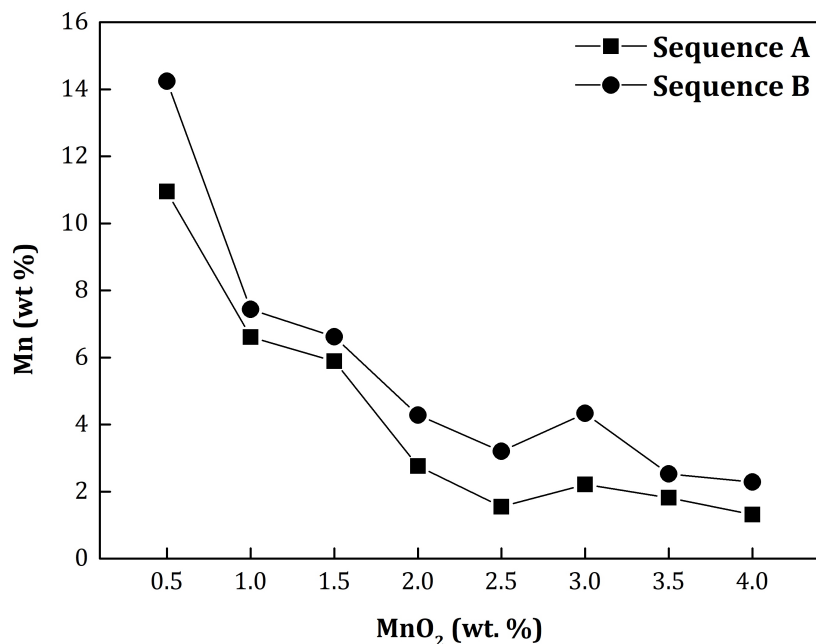


Figure 4.12: Manganese recovery in $Al - MnO_2$ system.

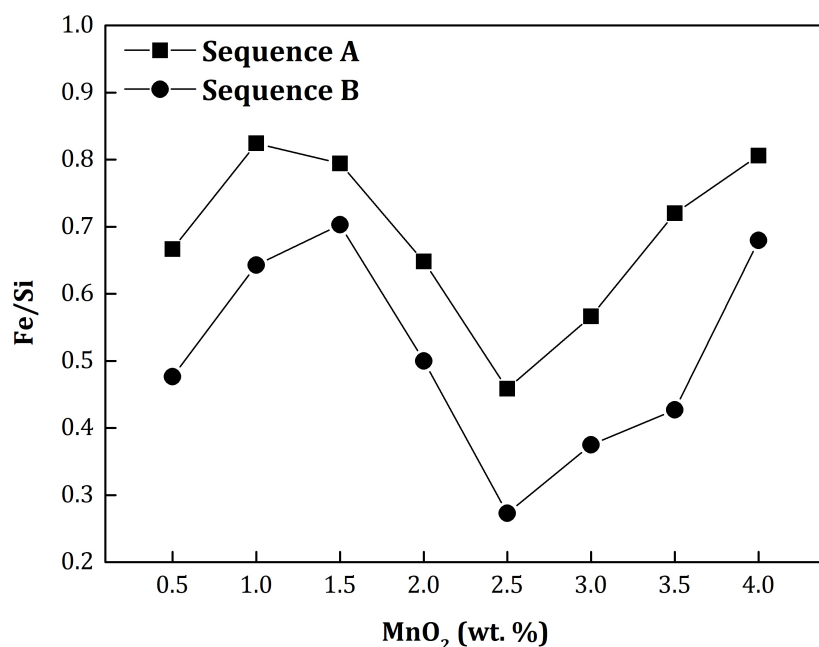


Figure 4.13: Fe/Si ratio of $Al - MnO_2$ system.

2. X-Ray Diffraction

In phase II experiments the optimization of MnO_2 in CPA, MnO_2 was checked by MnO_2 addition varies from 0.5 to 4 wt %. The X-Ray diffraction analysis of 2.5 wt % MnO_2 was carried out for sequence A and sequence B experiments as shown in figure 4.14 and figure 4.15. Table 4.8 and 4.9 shows typical peak values with respective phases.

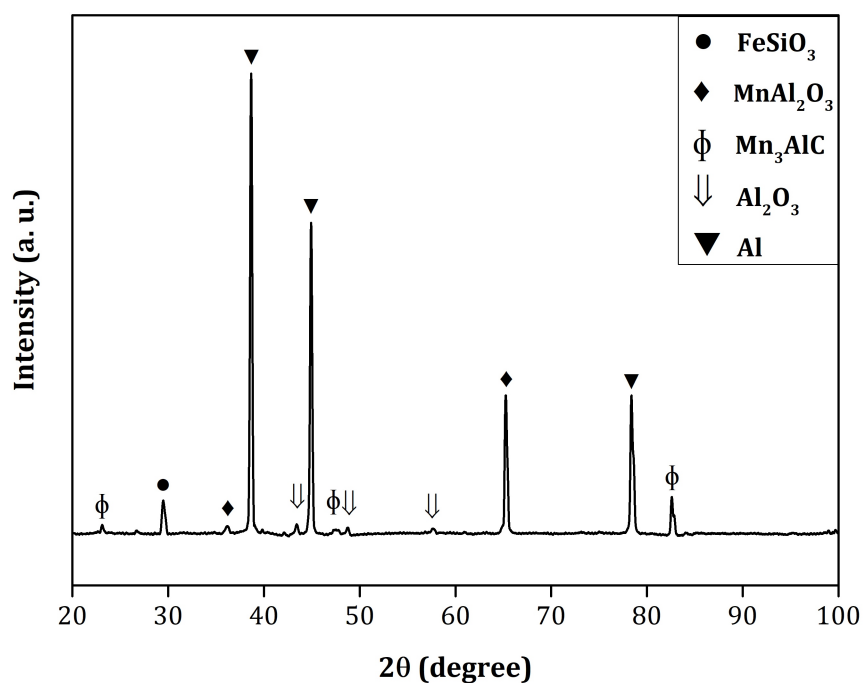


Figure 4.14: Typical XRD pattern of Al-2.5 wt % MnO_2 system in sequence A of Al – MnO_2 system.

Table 4.8: X-Ray diffraction values of Al-2.5 wt % MnO_2 system in sequence A.

Sr. No.	2-Theta	Observed d value	Phase	JCPDS Card No.
1	23.08	3.85	Mn_3AlC	7 – 124
2	29.46	3.03	$FeSiO_3$	17 – 548
3	36.15	2.48	$MnAl_2O_3$	10 – 310
4	38.56	2.33	Al	4 – 787
5	43.39	2.08	Al_2O_3	10 – 173
6	44.92	2.02	Al	4 – 787
7	47.55	1.91	Mn_3AlC	7 – 124
8	48.74	1.87	Al_2O_3	10 – 173
9	57.64	1.60	Al_2O_3	10 – 173
10	65.25	1.43	$MnAl_2O_3$	10 – 310
11	78.38	1.22	Al	4 – 787
12	82.59	1.17	Mn_3AlC	7 – 124

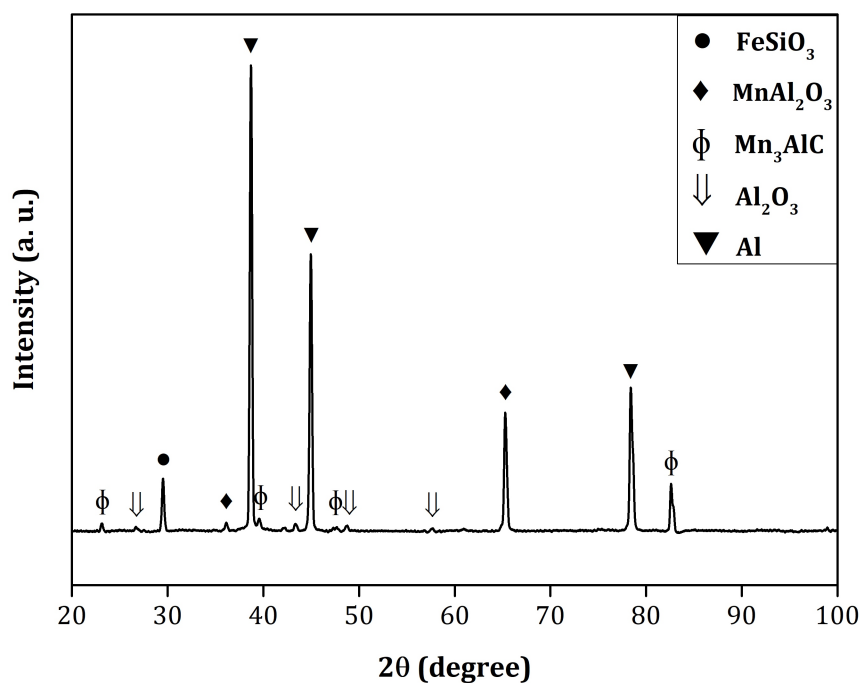


Figure 4.15: Typical XRD pattern of $Al - 2.5wt\%MnO_2$ system in sequence B of $Al - MnO_2$ system.

Table 4.9: X-Ray diffraction values of $Al-2.5$ wt % MnO_2 system in sequence B.

Sr. No.	2-Theta	Observed d value	Phase	JCPDS Card No.
1	23.13	3.84	Mn_3AlC	7 – 124
2	26.74	3.33	Al_2O_3	10 – 173
3	29.48	3.03	$FeSiO_3$	17 – 548
4	36.10	2.48	$MnAl_2O_3$	10 – 310
5	38.59	2.33	Al	4 – 787
6	39.54	2.28	Mn_3AlC	7 – 124
7	43.35	2.08	Al_2O_3	10 – 173
8	44.92	2.02	Al	4 – 787
9	47.52	1.91	Mn_3AlC	7 – 124
10	48.67	1.87	Al_2O_3	10 – 173
11	57.56	1.60	Al_2O_3	10 – 173
12	65.25	1.43	$MnAl_2O_3$	10 – 310
13	78.41	1.22	Al	4 – 787
14	82.61	1.17	Mn_3AlC	7 – 124

Typical X-Ray pattern indicates the presence of oxides and complex carbides such as $FeSiO_3$, $MnAl_2O_3$, Mn_3AlC and Al_2O_3 into the CPA matrix. Raw MnO_2 contained the carbon and hence in resultant in-situ composite the generation of complex carbides were seen. No peak was observed of MnO_2 which indicated all MnO_2 has been consumed for the formation of various compounds. Beyond 2.5 wt % MnO_2 , addition was very difficult. The density of MnO_2 powder is very less as compared to CPA, we found floating of these powder on CPA liquid bath. The rejection of MnO_2 powder by the liquid bath increased beyond 2.5 wt % level. This was the reason to choose only 2.5 wt % MnO_2 sample for XRD analysis for sequence B.

3. Density and ductility

As shown from figure 4.16, the density results were dropping from the initial value throughout the addition of MnO_2 in sequence A and B as per the trend line (data fitting line) but found minimum at 2.5 wt % MnO_2 . As confirmed from XRD analysis of 2.5 wt % MnO_2 , generation of various in-situ intermetallic phases such as $FeSiO_3$, $MnAl_2O_3$, Mn_3AlC and Al_2O_3 were observed. Among these in-situ intermetallic phases, amount of light but brittle phase Mn_3AlC is higher in sequence B based on peak numbers and peak height as compared to heavy phase $MnAl_2O_3$. Because of this fact, density value in 2.5 wt % MnO_2 of sequence B was found minimum compared to sequence A.

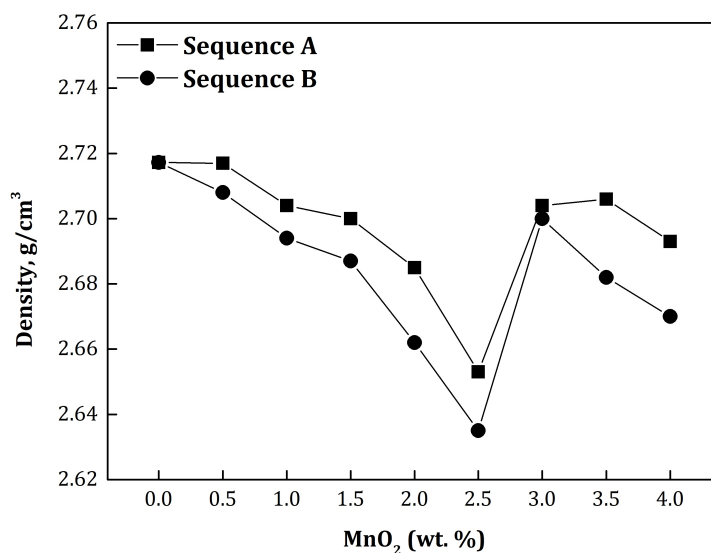


Figure 4.16: Variations of density in sequence A and sequence B of $Al - MnO_2$ system.

As we can see from figure 4.17, the trend line (data fitting line) of ductility values were found increasing in sequence B whereas it was decreasing in sequence A. At 2.5 wt % MnO_2 , the ductility was minimum in sequence B as compared to the sequence A. As mentioned above in density variation, generation of in-situ brittle phase Mn_3AlC is responsible for the same.

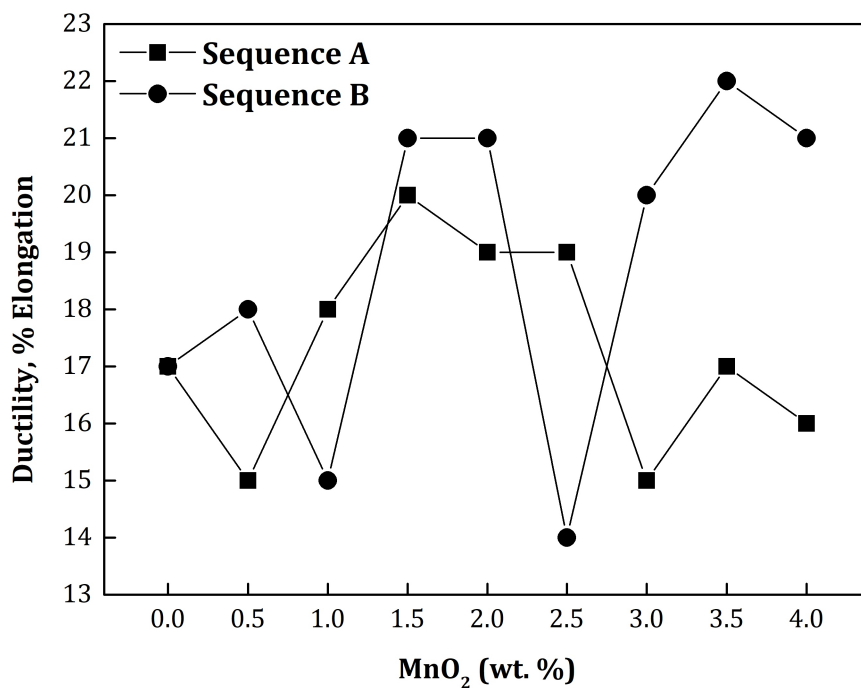


Figure 4.17: Variations of ductility in sequence A and sequence B of $Al - MnO_2$ system.

4. Hardness and strength

As shown from figure 4.18, hardness distribution remains almost unchanged in entire system as per the trend line in sequence A. But in sequence B, hardness value increases as amount of MnO_2 added.

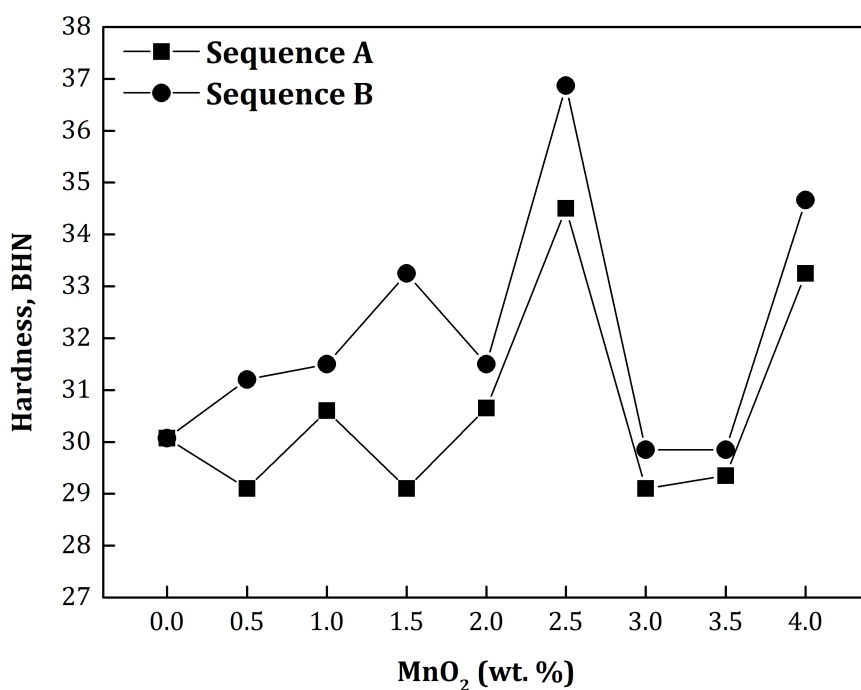


Figure 4.18: Variations of hardness in sequence A and sequence B of $Al - MnO_2$ system.

Similarly as indicated in figure 4.19, the slight reduction in ultimate tensile strength values were observed in sequence A while in sequence B, it increases as MnO_2 increases. Although the highest hardness values were observed in 2.5 wt % MnO_2 combination in the both sequences A and B whereas the highest UTS was found in sequence A at 2.5 wt % MnO_2 compositions and at 2 wt % MnO_2 in sequence B.

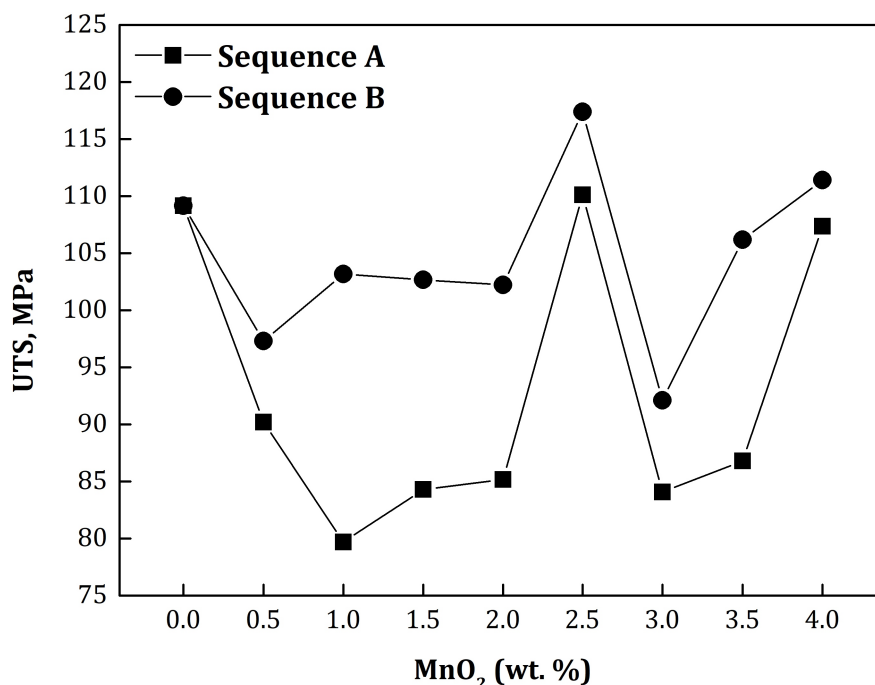


Figure 4.19: Variations of ultimate tensile strength in sequence A and sequence B of $Al - MnO_2$ system.

5. Microstructure

Microstructures shown in above figure 4.20 and figure 4.21 consist of results of both the sequence A and B. Compare to sequence A, sequence B microstructures show more uniformity as far as morphology of grain boundaries and other resultant phases (table 4.8 and 4.9) are concerned. By comparing both sequence results, the addition of MnO_2 as in sequence A gave more bulky grain boundaries and segregated phases whereas in sequence B thin grain boundaries are observed. The resultant phases are also well distributed in sequence B.

SEM images are shown in figure 4.22 and 4.23. As we can see, comparatively in sequence A, thin phases are observed whereas in sequence B, thick and uniform phases are observed due to more reaction time involved in sequence B. At 100x magnification, we can see the formation of in-situ phases are almost uniform in sequence B but in sequence A, discontinuous in-situ phases are found in small amount.

(a) Sequence A

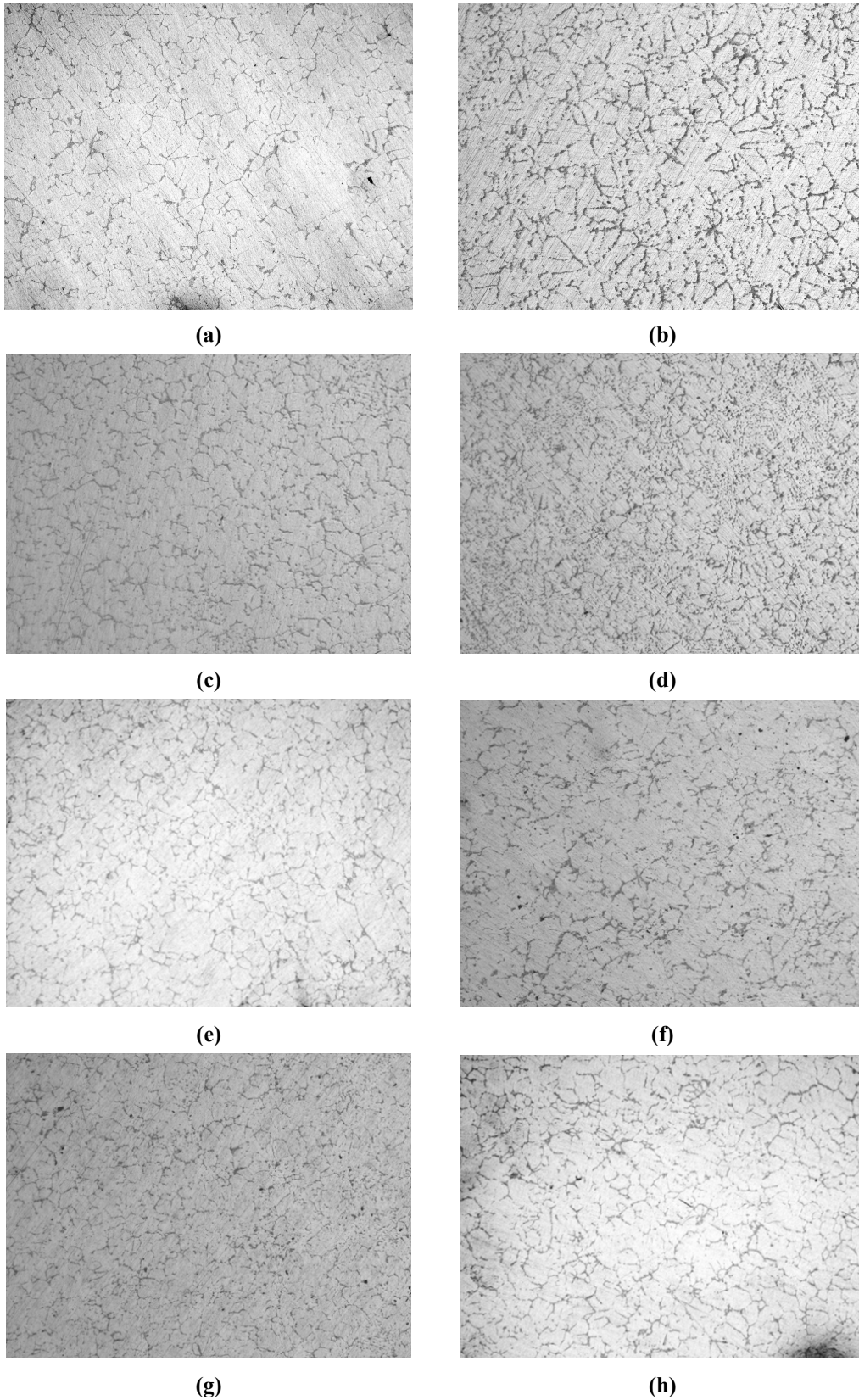


Figure 4.20: Sequence A Optical microstructure of (a) 0.5 wt % MnO_2 , (b) 1 wt % MnO_2 , (c) 1.5 wt % MnO_2 , (d) 2 wt % MnO_2 , (e) 2.5 wt % MnO_2 , (f) 3 wt % MnO_2 , (g) 3.5 wt % MnO_2 and (h) 4 wt % MnO_2 of $Al - MnO_2$ system at 100x magnification (Without Etching).

(b) Sequence B

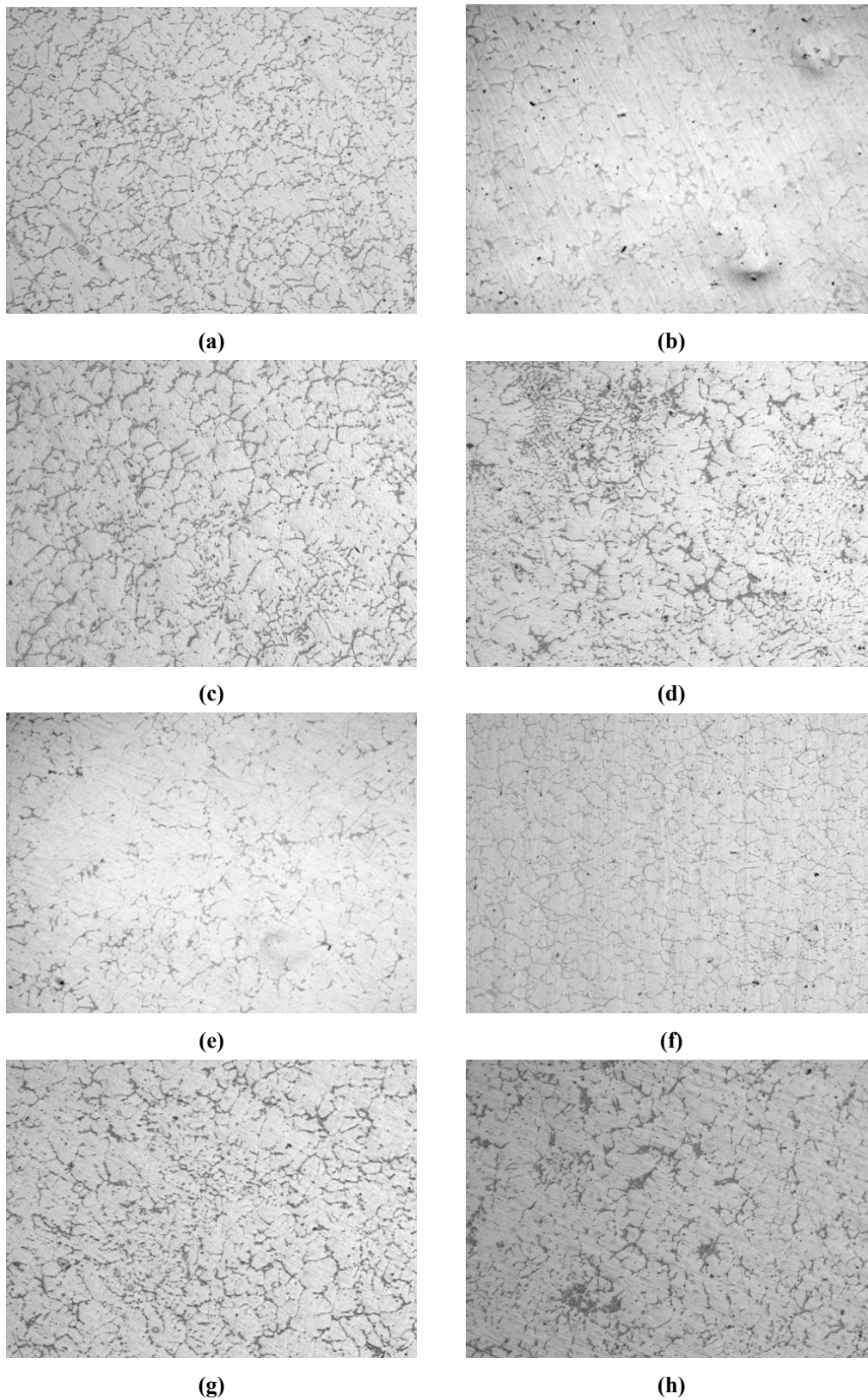


Figure 4.21: Sequence B Optical microstructure of (a) 0.5 wt % MnO_2 , (b) 1 wt % MnO_2 , (c) 1.5 wt % MnO_2 , (d) 2 wt % MnO_2 , (e) 2.5 wt % MnO_2 , (f) 3 wt % MnO_2 , (g) 3.5 wt % MnO_2 and (h) 4 wt % MnO_2 of $Al - MnO_2$ system at 100x magnification (Without Etching).

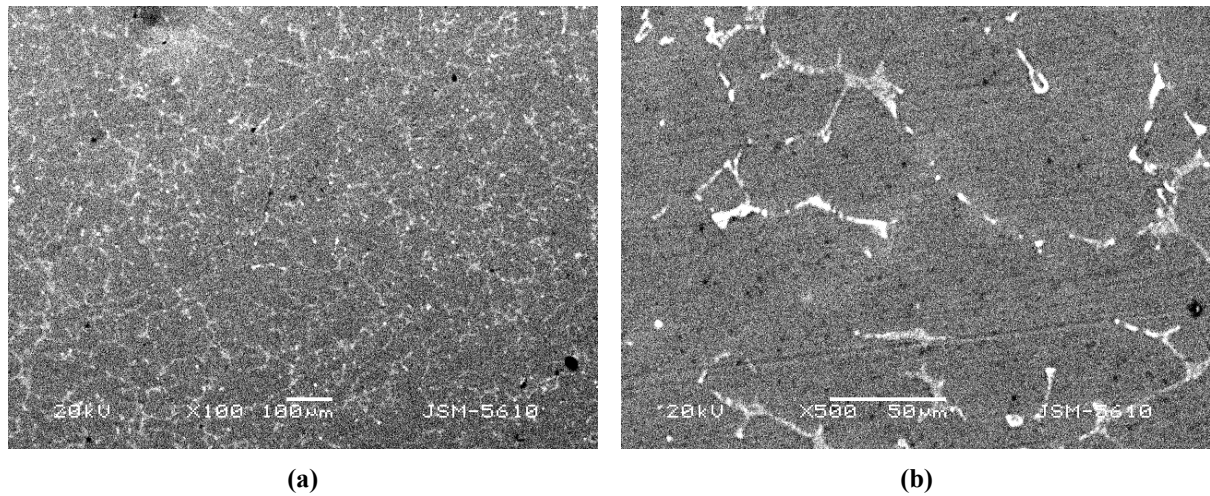


Figure 4.22: SEM images of 2.5 wt % MnO_2 in sequence A at (a) 100x and (b) 500x magnification (Without Etching).

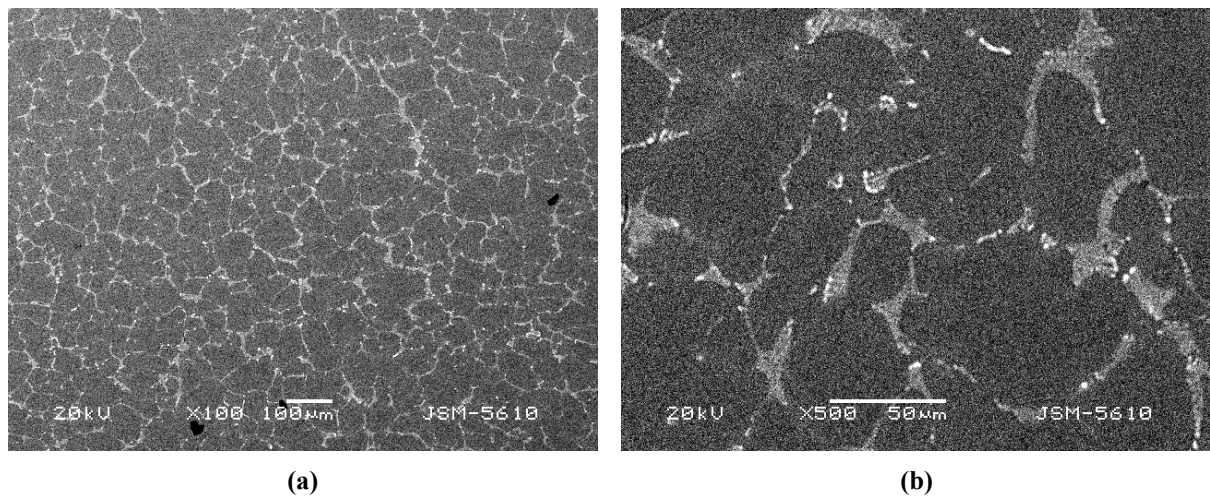


Figure 4.23: SEM images of 2.5 wt % MnO_2 in sequence B at (a) 100x and (b) 500x magnification (Without Etching).

4.2.3 Phase III: Effect of variation in MnO_2 by changing its addition sequence along with the optimised magnesium from phase I study.

In phase I, optimisation of magnesium was confirmed whereas in phase II, effect of MnO_2 in commercially pure aluminium was measured without any wetting agent. In phase III study, optimisation of MnO_2 reinforcement in Al - 3 wt % Mg system checked by changing its addition sequence. Detail experimental flow sheet is already mentioned in chapter 3.

1. Chemical analysis

Quantitative and qualitative analysis of various elements like Mg, Si, Mn and Fe recovered are as shown in table 4.10. It is observed that Si and Fe are presence in raw materials. It was found that Mg and Mn recoveries are higher in sequence B as compared to sequence A. Spectroscopy testing was performed for recovery results.

Table 4.10: Chemical compositions of various Al – Mg – MnO_2 systems by spectroscopy

Experiments	Mg added (wt %)	MnO_2 added (wt %)	Element Composition (wt %)				
			Mg	Mn	Si	Fe	Al
1 (CPA)	00	00	0.12	0.21	0.48	0.82	98.37
Sequence A*							
2	3	1.0	2.61	0.25	0.73	0.79	94.43
3	3	2.5	2.43	0.66	0.58	0.74	95.97
4	3	4.0	2.38	0.92	0.72	0.63	93.84
Sequence B [#]							
5	3	1.0	2.67	0.31	1.43	1.16	95.69
6	3	2.5	2.68	0.93	2.57	0.95	95.54
7	3	4.0	2.71	1.08	3.56	1.62	91.79

*Sequence A: MnO_2 added after melting of commercially pure aluminium and

[#]Sequence B: MnO_2 added before melting of commercially pure aluminium

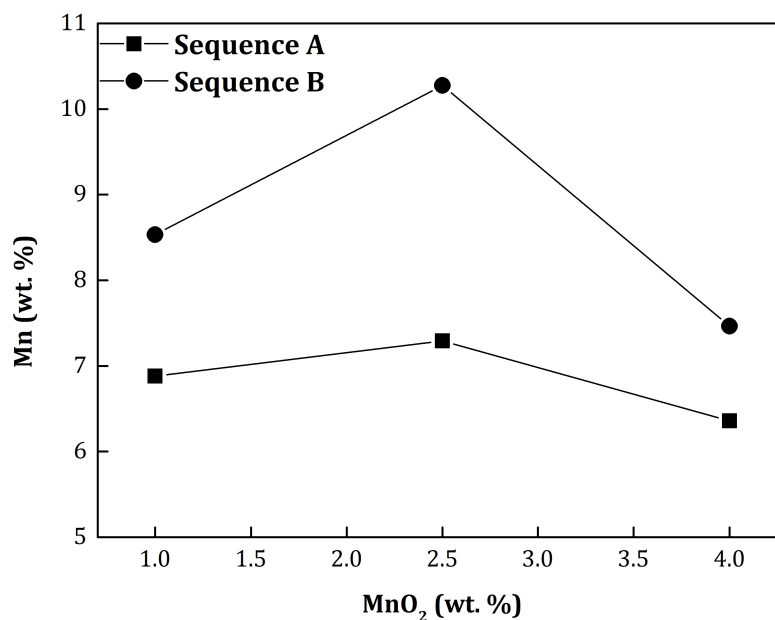


Figure 4.24: Mn recovery in sequence A and sequence B of Al – 3wt%Mg – MnO₂ system.

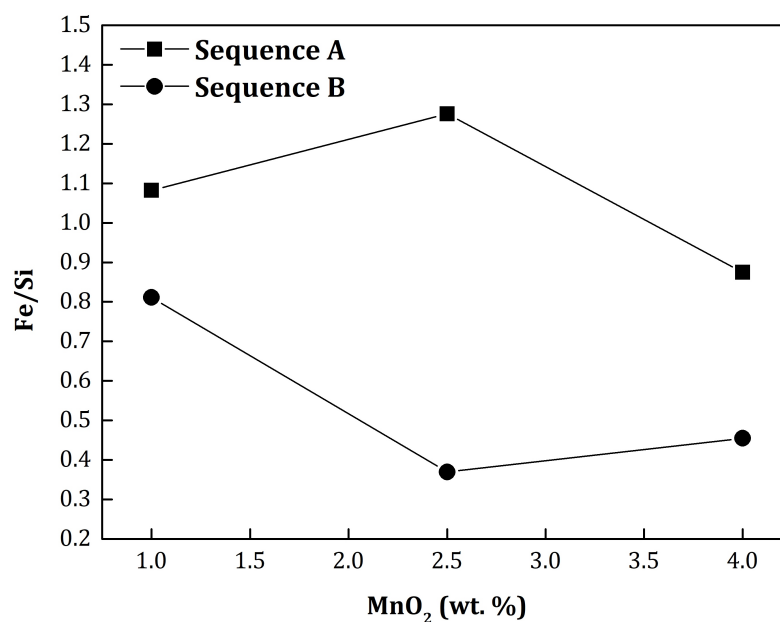


Figure 4.25: Fe/Si ratio of Al – 3wt%Mg – MnO₂ system.

2. X-Ray Diffraction

All X-Ray patterns show almost similar patterns and compounds peaks. The presence of the in-situ complex carbide compounds such as $Mg-Fe-SiO_3$, $MnAl_2O_3$, $Mg-Si-O$, Al_2O_3 , Mn_3AlC and Mg were confirmed in below XRD patterns. It was noted that the peak height of Mn_3AlC in 2.5 wt % MnO₂ of sequence B experiments are higher as compared to all the combinations of sequence A experiments. It could be the main reason to have improved mechanical properties in this system following sequence B.

(a) Sequence A

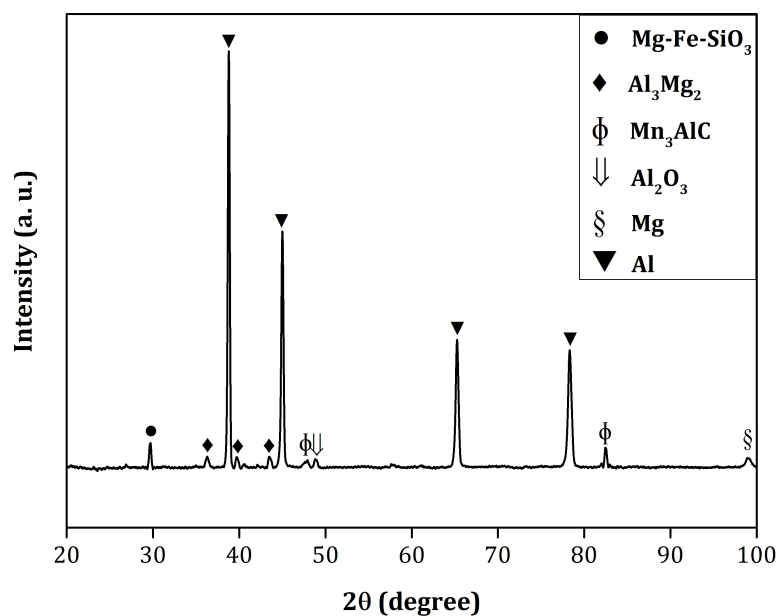


Figure 4.26: Typical X-ray diffraction patterns of 1 wt % MnO_2 in sequence A of $Al - 3wt\%Mg - MnO_2$ system.

Table 4.11: X-Ray diffraction values of $Al-1$ wt % MnO_2 system in sequence A.

Sr. No.	2-Theta	Observed d value	Phase	JCPDS Card No.
1	29.65	3.01	$Mg - Fe - SiO_3$	24 - 201
2	36.22	2.48	Al_3Mg_2	18 - 34
3	38.78	2.32	Al	4 - 787
4	39.69	2.27	Al_3Mg_2	18 - 34
5	43.46	2.08	Al_3Mg_2	18 - 34
6	44.98	2.01	Al	4 - 787
7	47.76	1.90	Mn_3AlC	7 - 124
8	48.82	1.86	Al_2O_3	10 - 173
9	65.26	1.43	Al	4 - 787
10	78.19	1.22	Al	4 - 787
11	82.49	1.17	Mn_3AlC	7 - 124
12	98.98	1.01	Mg	4 - 770

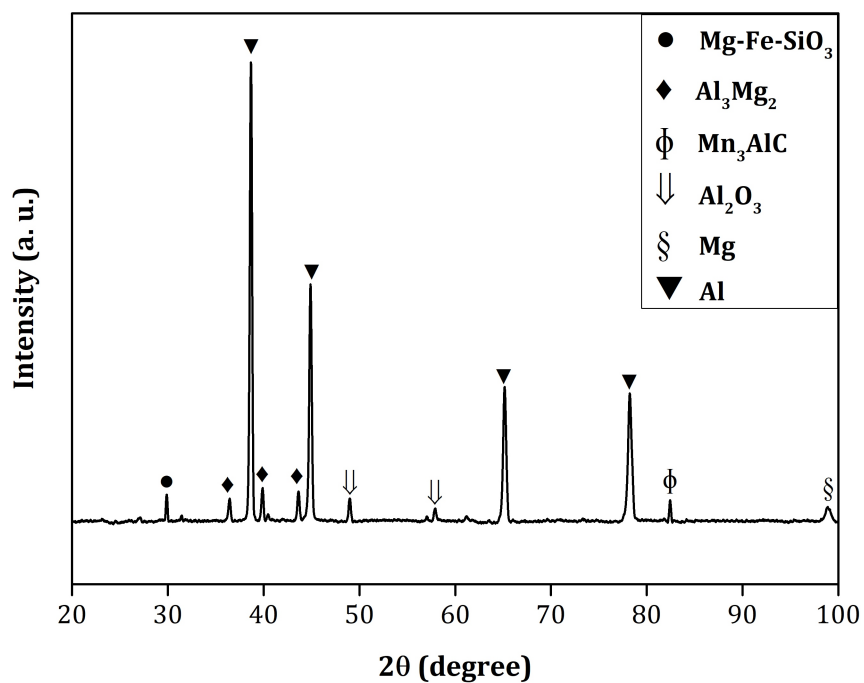


Figure 4.27: Typical X-ray diffraction patterns of 2.5 wt % MnO_2 in sequence A of $Al - 3wt\%Mg - MnO_2$ system.

Table 4.12: X-Ray diffraction values of $Al-2.5$ wt % MnO_2 system in sequence A.

Sr. No.	2-Theta	Observed d value	Phase	JCPDS Card No.
1	29.87	2.99	$Mg - Fe - SiO_3$	24 - 201
2	36.40	2.47	Al_3Mg_2	18 - 34
3	38.66	2.33	Al	4 - 787
4	39.86	2.26	Al_3Mg_2	18 - 34
5	43.60	2.07	Al_3Mg_2	18 - 34
6	44.84	2.02	Al	4 - 787
7	48.93	1.86	Al_2O_3	10 - 173
8	57.83	1.59	Al_2O_3	10 - 173
9	65.12	1.43	Al	4 - 787
10	78.14	1.22	Al	4 - 787
11	82.35	1.17	Mn_3AlC	7 - 124
12	98.78	1.01	Mg	4 - 770

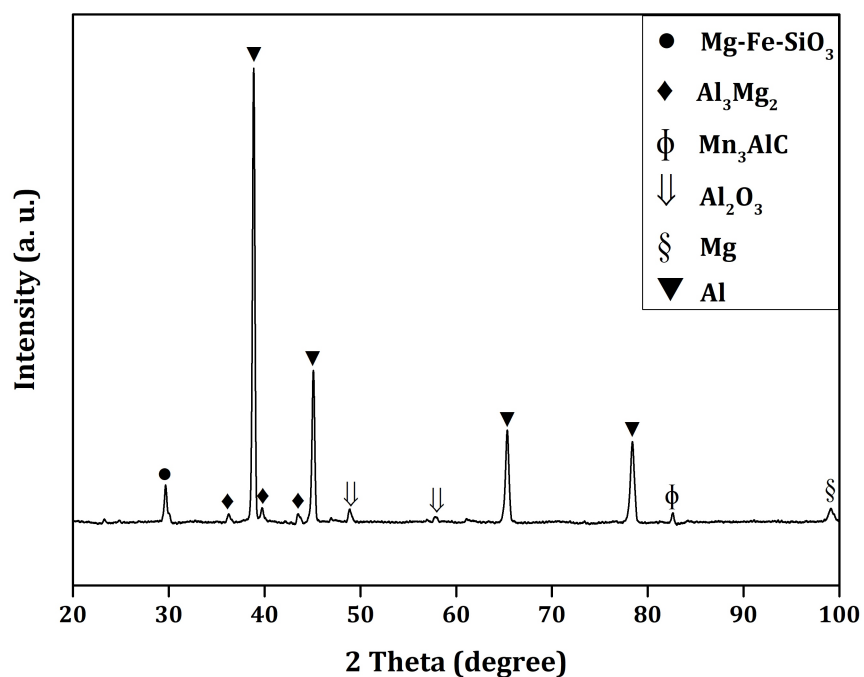


Figure 4.28: Typical X-ray diffraction patterns of 4 wt % MnO_2 in sequence A of $Al - 3wt\%Mg - MnO_2$ system.

Table 4.13: X-Ray diffraction values of $Al-4$ wt % MnO_2 system in sequence A.

Sr. No.	2-Theta	Observed d value	Phase	JCPDS Card No.
1	29.66	3.01	$Mg - Fe - SiO_3$	24 - 201
2	36.22	2.48	Al_3Mg_2	18 - 34
3	38.84	2.32	Al	4 - 787
4	39.70	2.27	Al_3Mg_2	18 - 34
5	43.47	2.08	Al_3Mg_2	18 - 34
6	45.05	2.01	Al	4 - 787
7	48.83	1.86	Al_2O_3	10 - 173
8	57.76	1.59	Al_2O_3	10 - 173
9	65.29	1.43	$MnAl_2O_3$	10 - 310
10	78.33	1.22	Al	4 - 787
11	82.62	1.17	Mn_3AlC	7 - 124
12	98.99	1.01	Mg	4 - 770

(b) Sequence B

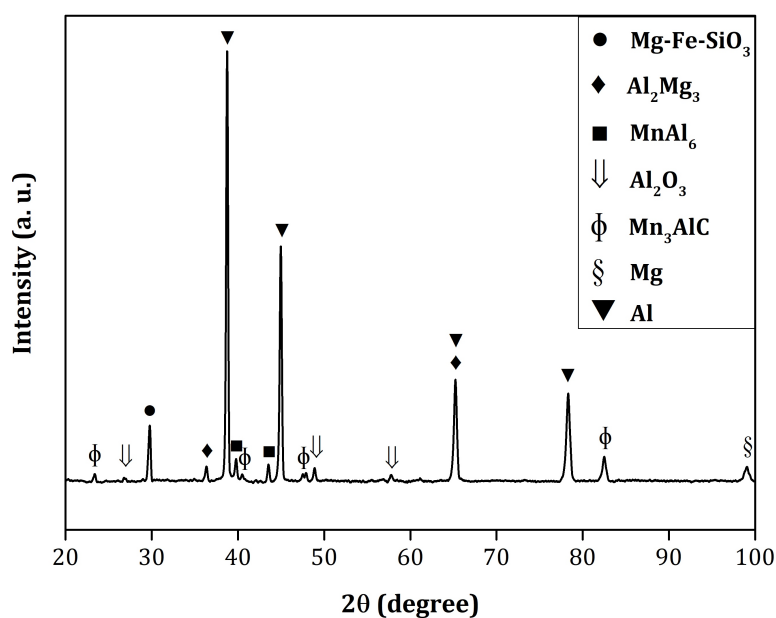


Figure 4.29: Typical X-ray diffraction patterns of 1 wt % MnO_2 in sequence B of $Al - 3wt\%Mg - MnO_2$ system.

Table 4.14: X-Ray diffraction values of Al-1 wt % MnO_2 system in sequence B.

Sr. No.	2-Theta	Observed d value	Phase	JCPDS Card No.
1	23.40	3.80	Mn_3AlC	7 – 124
2	26.86	3.32	Al_2O_3	10 – 173
3	29.76	3.00	$Mg - Fe - SiO_3$	24 – 201
4	36.31	2.47	Al_2Mg_3	1 – 1128
5	38.72	2.32	Al	4 – 787
6	39.77	2.26	$MnAl_6$	6 – 665
7	40.46	2.23	Mn_3AlC	7 – 124
8	43.51	2.08	$MnAl_6$	6 – 665
9	44.83	2.02	Al	4 – 787
10	47.85	1.90	Mn_3AlC	7 – 124
11	48.84	1.86	Al_2O_3	10 – 173
12	57.72	1.60	Al_2O_3	10 – 173
13	65.20	1.43	Al	4 – 787
14	65.20	1.43	Al_2Mg_3	1 – 1128
15	78.26	1.22	Al	4 – 787
16	82.41	1.17	Mn_3AlC	7 – 124
17	98.94	1.01	Mg	4 – 770

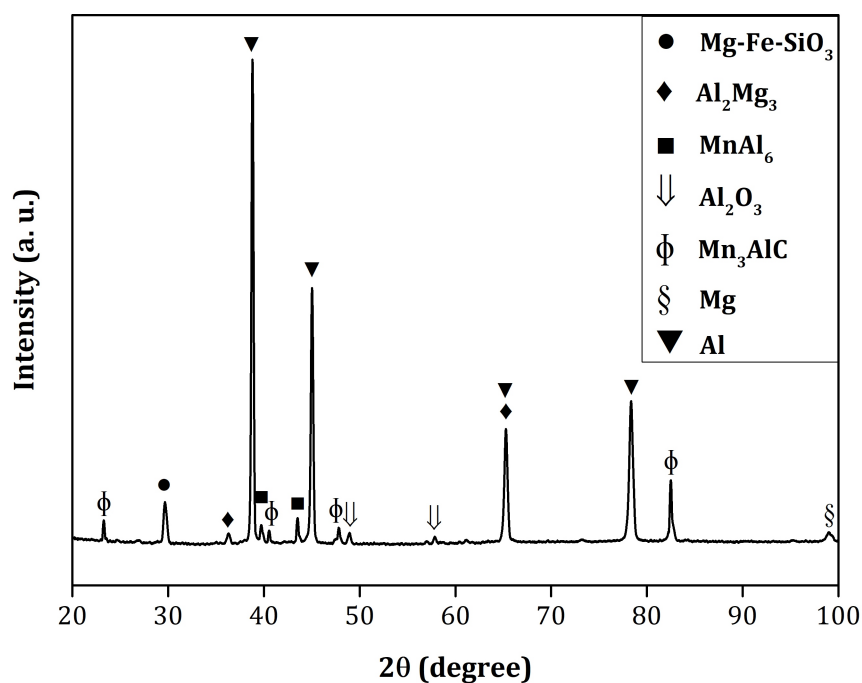


Figure 4.30: Typical X-ray diffraction patterns of 2.5 wt % MnO_2 in sequence B of $Al - 3wt\%Mg - MnO_2$ system.

Table 4.15: X-Ray diffraction values of $Al-2.5$ wt % MnO_2 system in sequence B.

Sr. No.	2-Theta	Observed d value	Phase	JCPDS Card No.
1	23.30	3.82	Mn_3AlC	7 – 124
2	29.63	3.01	$Mg - Fe - SiO_3$	24 – 201
3	36.26	2.48	Al_2Mg_3	1 – 1128
4	38.78	2.32	Al	4 – 787
5	39.70	2.27	$MnAl_6$	6 – 665
6	40.56	2.22	Mn_3AlC	7 – 124
7	43.51	2.08	$MnAl_6$	6 – 665
8	44.98	2.01	Al	4 – 787
9	47.83	1.90	Mn_3AlC	7 – 124
10	48.90	1.86	Al_2O_3	10 – 173
11	57.78	1.59	Al_2O_3	10 – 173
12	65.24	1.43	Al	4 – 787
13	65.24	1.43	Al_2Mg_3	1 – 1128
14	78.27	1.22	Al	4 – 787
15	82.49	1.17	Mn_3AlC	7 – 124
16	98.97	1.01	Mg	4 – 770

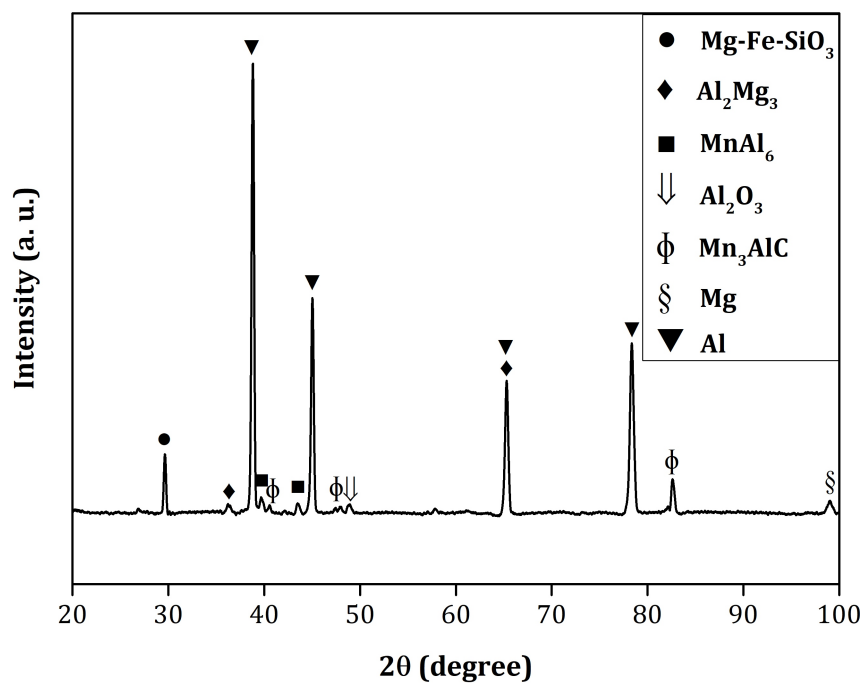


Figure 4.31: Typical X-ray diffraction patterns of 4 wt % MnO_2 in sequence B of $Al - 3wt\%Mg - MnO_2$ system.

Table 4.16: X-Ray diffraction values of $Al-4$ wt % MnO_2 system in sequence B.

Sr. No.	2-Theta	Observed d value	Phase	JCPDS Card No.
1	29.6	3.02	$Mg - Fe - SiO_3$	24 - 201
2	36.20	2.48	Al_2Mg_3	1 - 1128
3	38.79	2.32	Al	4 - 787
4	39.68	2.27	$MnAl_6$	6 - 665
5	40.52	2.22	Mn_3AlC	7 - 124
6	43.46	2.08	$MnAl_6$	6 - 665
7	44.99	2.01	Al	4 - 787
8	47.71	1.90	Mn_3AlC	7 - 124
9	48.81	1.86	Al_2O_3	10 - 173
10	65.27	1.43	Al	4 - 787
11	65.27	1.43	Al_2Mg_3	1 - 1128
12	78.28	1.22	Al	4 - 787
13	82.44	1.17	Mn_3AlC	7 - 124
14	98.92	1.01	Mg	4 - 770

3. Density and ductility

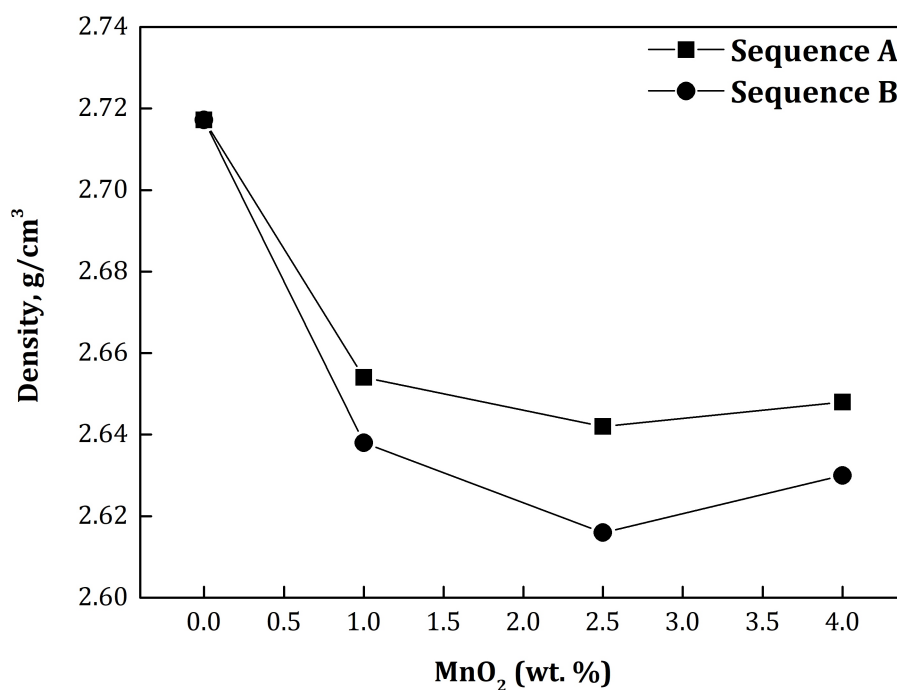


Figure 4.32: Variations of density in sequence A and B of $Al - 3wt\%Mg - MnO_2$ system.

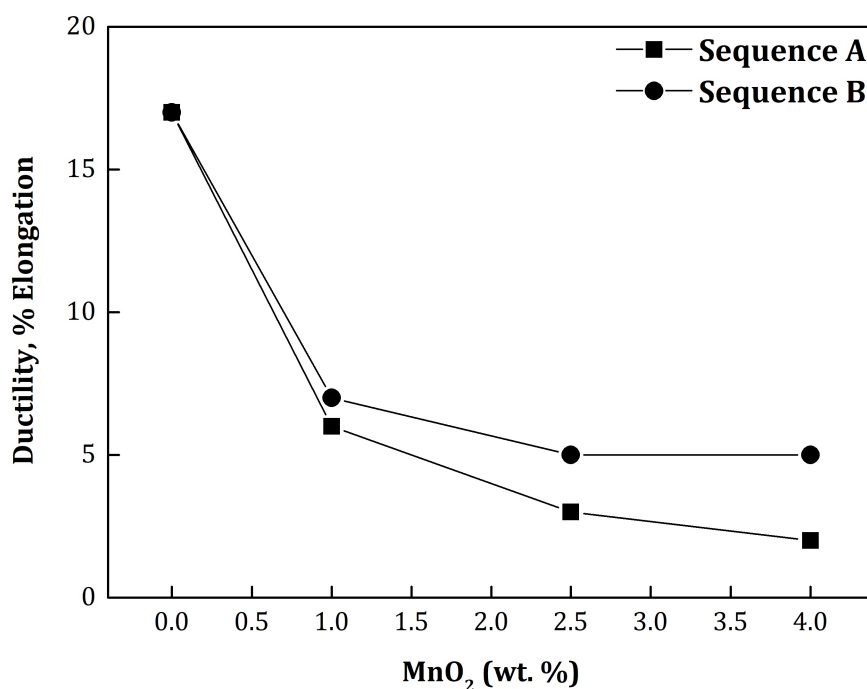


Figure 4.33: Variations of ductility in sequence A and B of $Al - 3wt\%Mg - MnO_2$ system.

Density was found by Pycnometer instrument as shown in figure 3.17. Density variation is shown in figure 4.32. Cylindrical samples were prepared of 20 mm diameter and 20 mm height. Presence of heavier and lighter phases in the matrix affects the level of density

values of resultant composite material. In sequence B, lowest density was observed due to formation of light Al_2Mg_3 (molecular weight is 126.88 gm/mole) in-situ phase. In sequence A, formation of Al_3Mg_2 were observed which is comparatively heavier (molecular weight is 129.56 gm/mole) as indicated in XRD analysis. Beyond 2.5 wt % MnO_2 addition, density values were increased in both the sequences A and B as shown in figure 4.32. Porosity was not considered in entire study. However, porosity plays a vital role in density variations. In present investigation, no evidence of porosity was found as per the microstructures. Stirring speed and degassing method can control the porosity values.

Ductility was measured in terms of percentage of elongations in the tensile samples as shown in figure 4.33. Ductility values are found decreasing as the amount of MnO_2 addition increased. This was due to formation of hard phases in the matrix. Lowest reading of the ductility was noted in sequence A experiments. Overall both ductility and density were marginally lowered in both sequences A and B as compared to the base matrix material.

4. Hardness and strength

Variations of hardness property with respect to MnO_2 amount for both sequences A and B are shown in figure 4.34. In both A and B sequences, similar pattern of incremental hardness were reported upto 2.5 wt % MnO_2 addition. Afterwards, hardness values were reduced. Maximum value of hardness property was reported in sequence B at 2.5 wt % MnO_2 .

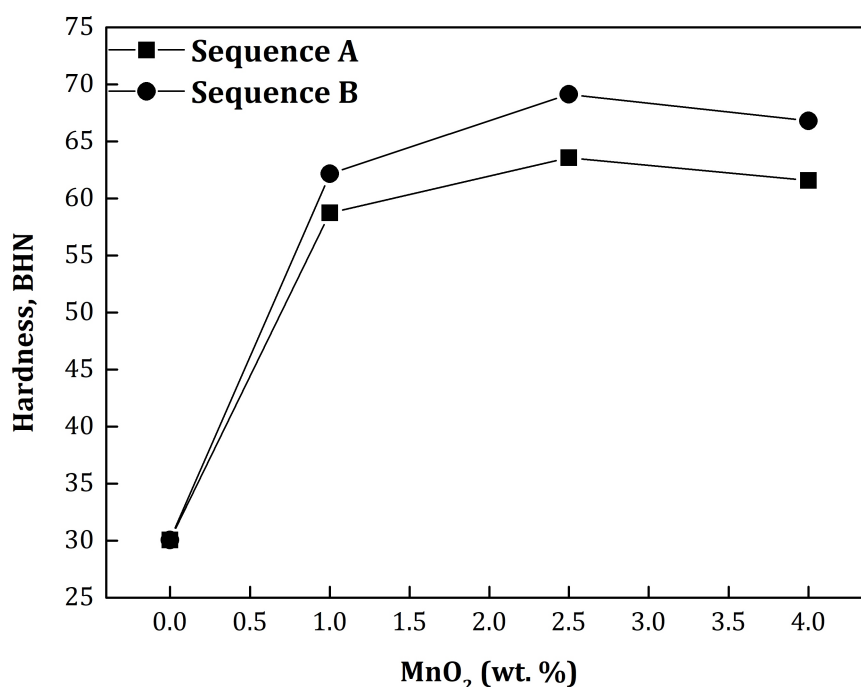


Figure 4.34: Variations of hardness in sequence A and B of $Al - 3wt\%Mg - MnO_2$ system.

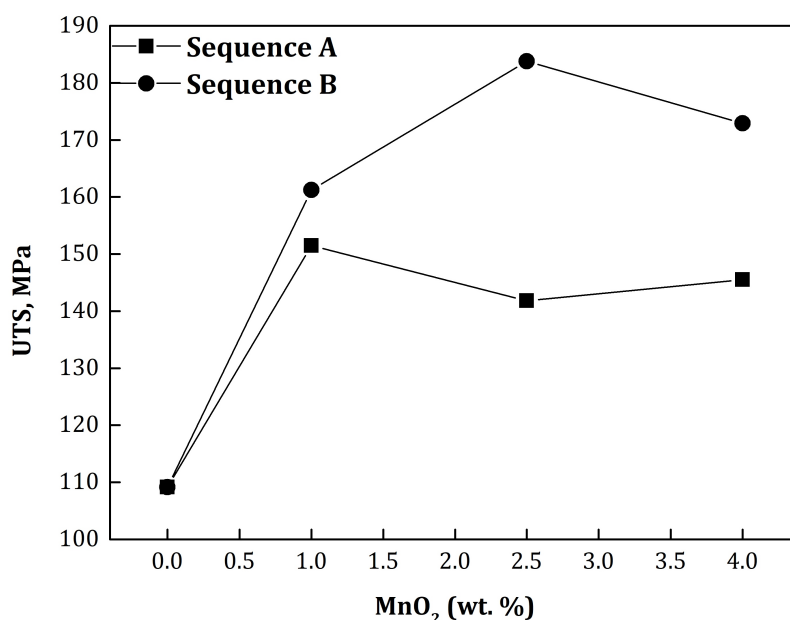


Figure 4.35: Variations of ultimate tensile strength in sequence A and B of $Al - 3wt\%Mg - MnO_2$ system.

Figure 4.35 shows the variation of tensile strength values with respect to different wt% of MnO_2 additions. Tensile testing was performed on Monsanto 20 tensile testing machine at the cross head speed of 0.05 mm/ min. It can be seen that in sequence A, the tensile strength results are decreasing and found minimum at 2.5 wt % MnO_2 while in sequence B, the results are marginally higher and found maximum at 2.5 wt % MnO_2 . Both hardness and tensile strength results in sequence B are found higher mainly due to in-situ formation of $MnAl_6$ along with cemented carbide Mn_3AlC . Formation of such phases is due to higher interaction time between MnO_2 and aluminium as it was added before melting of CPA. It means in sequence B, during entire melting procedure from room temperature to processing temperature, MnO_2 powder had more time to interact with CPA from mushy stage to liquid stage. The presence of fine dispersoids in the soft aluminium matrix, acts as the barriers in the motion of dislocations. Thus it results into the dispersion strengthening which can be easily justified using classical Orowan theory. This phenomenon increases the flow stress of the entire composite system. The strengthening is generally found maximum where fine dispersoids are well distributed in the matrix.

5. Microstructure

The optical microstructures of sequence A and B composites are shown in figure 4.36 and 4.38 whereas SEM microstructures of sequence A and B are shown in figure 4.37 and 4.39 respectively. It indicate the fineness of the intermetallics which were formed during processing. Precipitation and segregation of various Al-Mn intermetallics and carbide compounds were observed in the microstructures. Comparatively, in sequence B

the intermetallics observed are well distributed throughout the matrix. In 1 wt % and 4 wt % MnO_2 , more dense segregation was observed than that of in 2.5 wt % MnO_2 systems. In sequences A and B, due to controlled parameter and proper degassing, no porosity was observed. Microstructural heterogeneity was found among the generated in-situ phases in sequence A as compared to sequence B microstructure results as illustrated. In sequence B, homogeneous distribution of in-situ phases was observed. In 2.5 wt % MnO_2 microstructure result shows more uniform distribution of fine dispersoids in the aluminium matrix.

Microstructures of $Al - 3wt\%Mg - MnO_2$ system were prepared by following standard metallographic practice without etching. In the microstructure, highest refinement was observed in $Al - 3wt\%Mg - 2.5wt\%MnO_2$ system in sequence B as shown in figure 4.38. More phase formation appeared in $Al - 3wt\%Mg - 1wt\%MnO_2$. Also the distribution of Al-Mn complex carbide was found uniform.

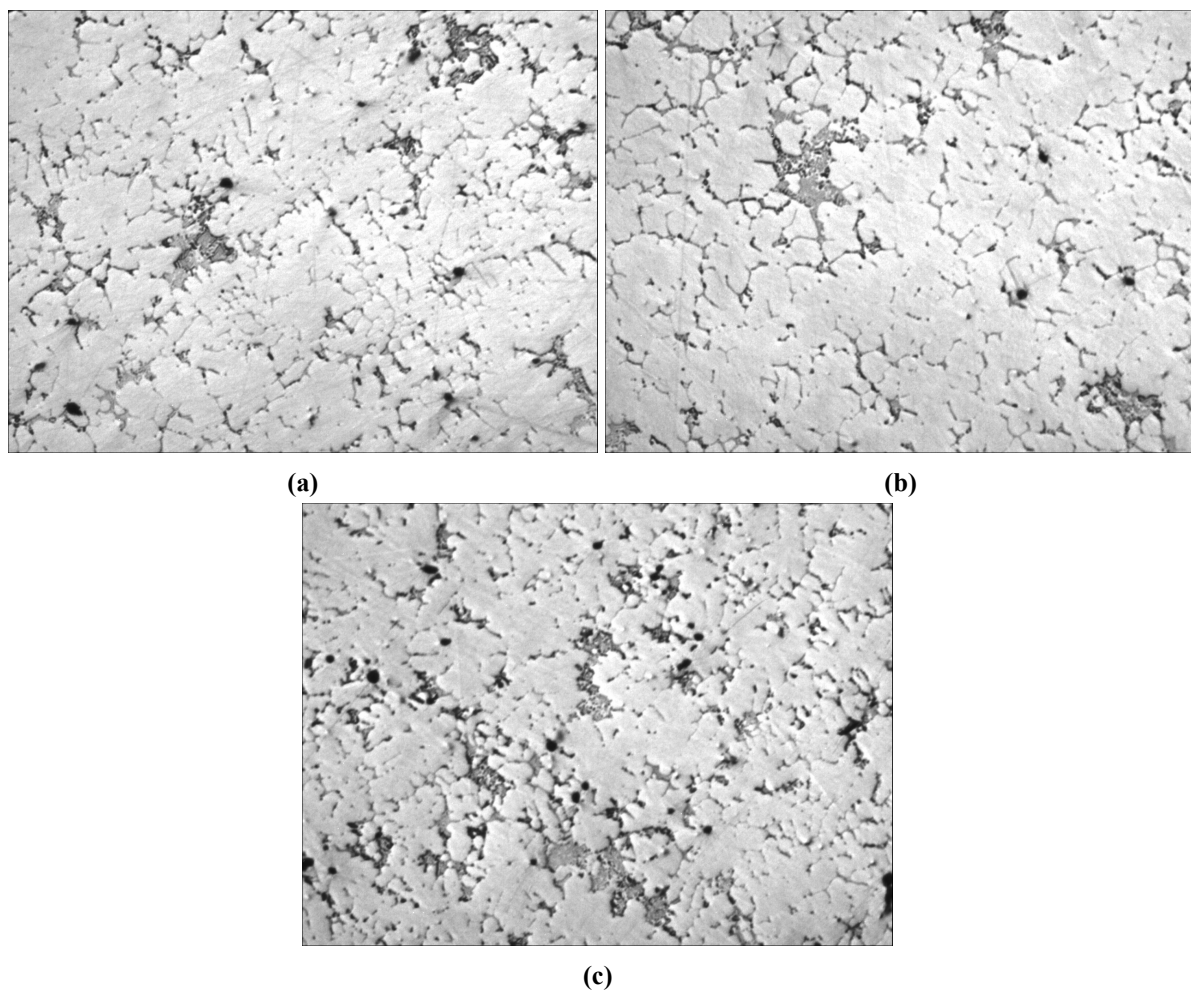
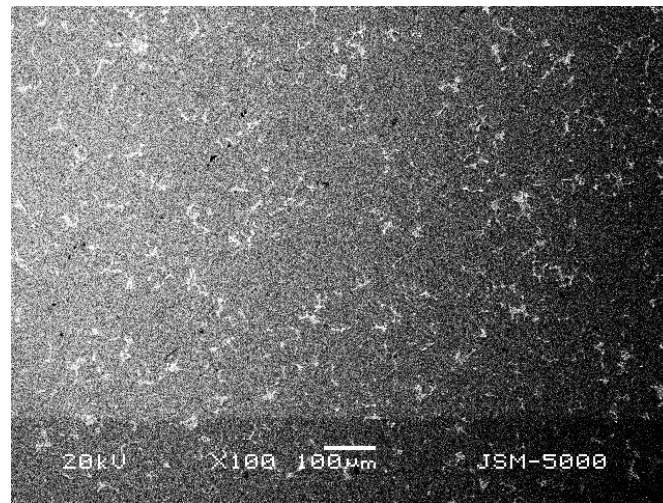
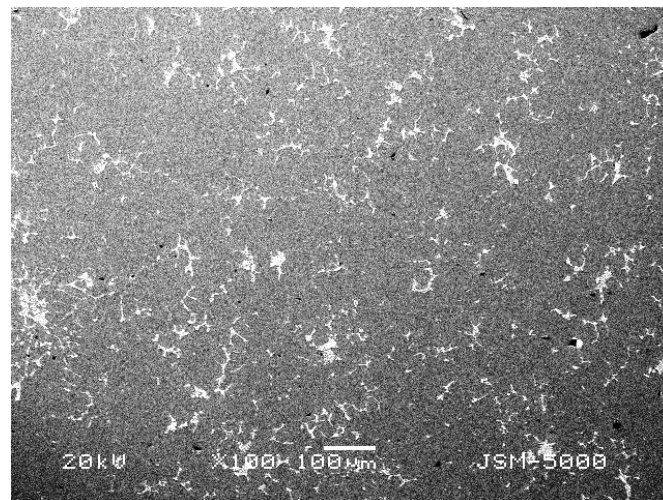


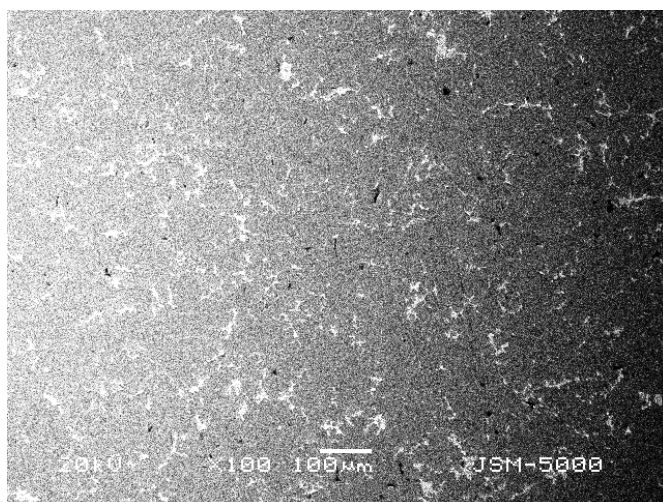
Figure 4.36: Optical microstructure of (a) 1 wt % MnO_2 , (b) 2.5 wt % MnO_2 and (c) 4 wt % MnO_2 of $Al - 3wt\%Mg - MnO_2$ system at 100x in sequence A (Without Etching).



(a)

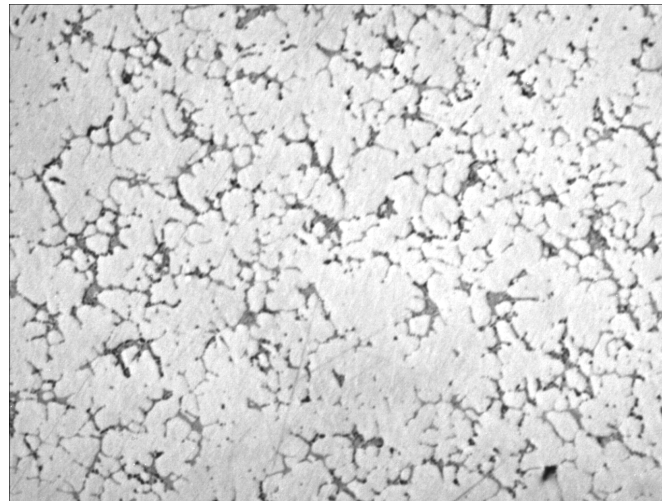


(b)

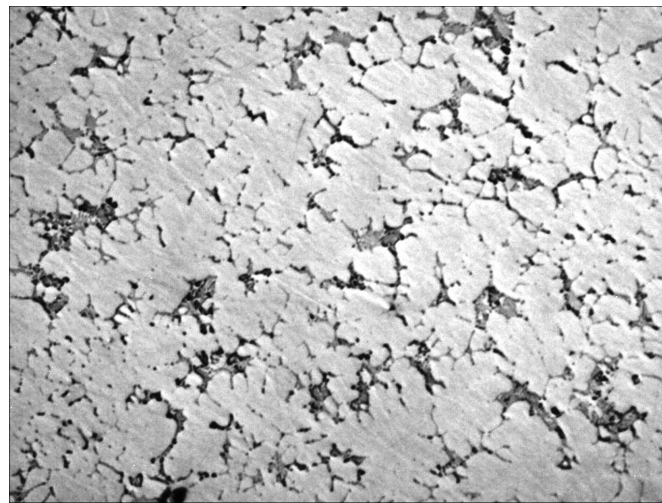


(c)

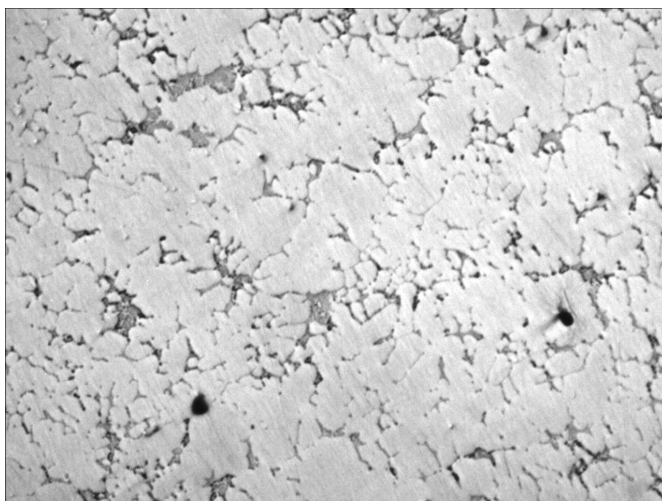
Figure 4.37: SEM images of (a) 1 wt % MnO_2 , (b) 2.5 wt % MnO_2 and (c) 4 wt % MnO_2 of $Al - 3wt\%Mg - MnO_2$ system at 100x in sequence A (Without Etching).



(a)

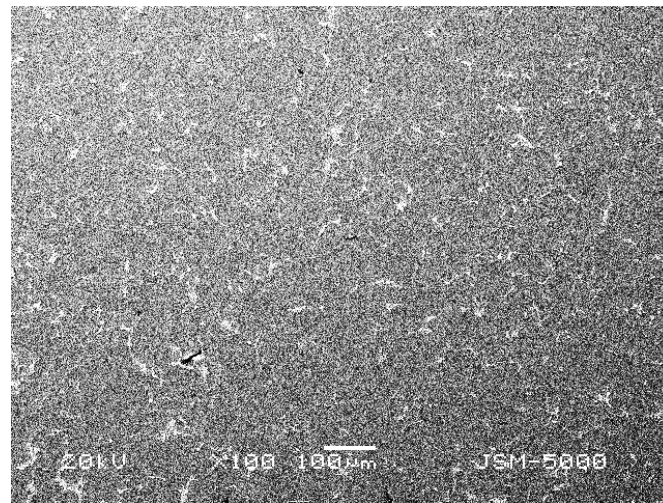


(b)

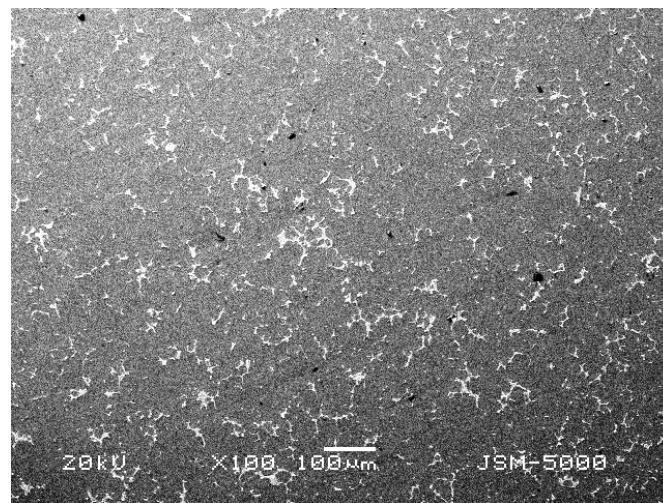


(c)

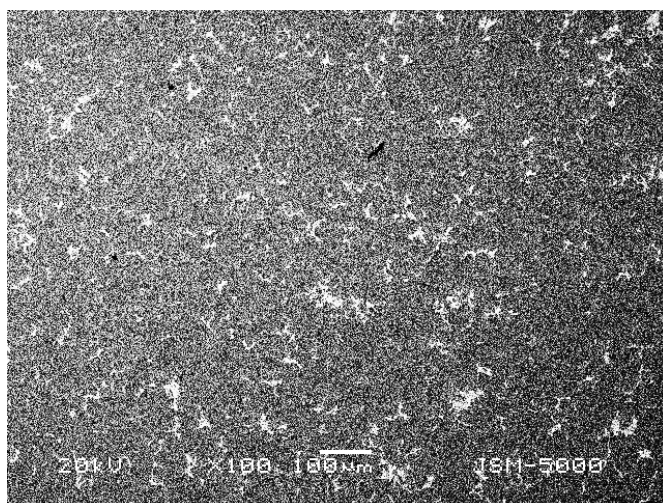
Figure 4.38: Optical microstructure of (a) 1 wt % MnO_2 , (b) 2.5 wt % MnO_2 and (c) 4 wt % MnO_2 of Al – 3wt%Mg – MnO_2 system at 100x in sequence B (Without Etching).



(a)



(b)



(c)

Figure 4.39: SEM images of (a) 1 wt % MnO_2 , (b) 2.5 wt % MnO_2 and (c) 4 wt % MnO_2 of Al – 3wt%Mg – MnO_2 system at 100x in sequence B (Without Etching).